

LARGE EDDY SIMULATION OF OSCILLATING AND  
DEFORMING AIRFOILS

LESLIE TAYLOR

A THESIS  
IN  
THE DEPARTMENT  
OF  
MECHANICAL, INDUSTRIAL AND AEROSPACE ENGINEERING

PRESENTED IN PARTIAL FULFILLMENT OF THE REQUIREMENTS  
FOR THE DEGREE OF MASTER OF APPLIED SCIENCE IN MECHANICAL  
ENGINEERING  
CONCORDIA UNIVERSITY  
MONTRÉAL, QUÉBEC, CANADA

AUGUST 2018

© LESLIE TAYLOR, 2018

CONCORDIA UNIVERSITY  
School of Graduate Studies

This is to certify that the thesis prepared

By: **Leslie Taylor**

Entitled: **Large Eddy Simulation of Oscillating and Deforming Air-foils**

and submitted in partial fulfillment of the requirements for the degree of

**Master of Applied Science in Mechanical Engineering**

complies with the regulations of this University and meets the accepted standards with respect to originality and quality.

Signed by the final examining committee:

\_\_\_\_\_ Chair  
Dr. Samuel Li \_\_\_\_\_ Examiner  
Dr. Brian Vermeire \_\_\_\_\_ Examiner  
Dr. Marius Paraschivoiu \_\_\_\_\_ Supervisor

Approved \_\_\_\_\_  
Chair of Department or Graduate Program Director

\_\_\_\_\_ 2018 \_\_\_\_\_

Dean

Faculty of Engineering and Computer Science

# Abstract

## Large Eddy Simulation of Oscillating and Deforming Airfoils

Leslie Taylor

This study examines the aerodynamic features of oscillating and deforming airfoils with vertical axis wind turbine applications. An in-house large eddy simulation (LES) computational fluid dynamic code with the wall-adapting local eddy viscosity sub-grid scale model is used to perform simulations, first to replicate the results of a water tunnel experiment studying an oscillating airfoil, and second to analyze the effects of airfoil deformation on aerodynamic properties.

The main features shown in the water tunnel experiments at a Reynolds number of 10,000 are present in the results of the simulations, including separation bubbles and laminar to turbulent transition, showing the effectiveness of using LES to simulate dynamic stall.

The deformation of the airfoil's trailing edge is implemented using a spring-based mesh deformation method, showing the effects of this movement on the airfoil's pressure coefficient.

# Acknowledgments

Thank you to my supervisor, Prof. Marius Paraschivoiu, for all of your scientific guidance and feedback.

A very special thank you to Dr. Matin Komeili for all of your help and patience, especially with the in-house code.

Thank you as well to the other members of the research group: Alex Leonczuk Minetto, Maryam Zabarjad, and Dan McLean.

And finally, thank you to Mathew Juhos for all of your encouragement.

I would also like to acknowledge Compute Canada and Calcul Quebec for the computing resources provided to me. These simulations could not have run without them.

# Contents

<b>1</b>	<b>Introduction</b>	<b>12</b>
1.1	Overview . . . . .	12
1.1.1	Wind Energy Today . . . . .	13
1.1.2	VAWT Aerodynamic Considerations . . . . .	16
1.1.3	Simulations of VAWT Aerodynamics . . . . .	16
1.1.4	Potential Improvements . . . . .	17
1.2	Contributions . . . . .	17
1.3	Thesis Contents . . . . .	19
<b>2</b>	<b>Theory and Literature Review</b>	<b>20</b>
2.1	Effects of Airfoil Aerodynamics on VAWT Power Production . . . . .	20
2.2	Static Versus Dynamic Stall . . . . .	21
2.2.1	The Dynamic Stall Process . . . . .	22
2.2.2	Factors Affecting the Dynamic Stall Process . . . . .	24
2.2.3	Mach Number Effects . . . . .	26
2.3	Dynamic Stall Simulation . . . . .	27
2.3.1	Numerical Methods . . . . .	27
2.3.2	RANS Models . . . . .	27
2.3.3	Large Eddy Simulation . . . . .	28
2.3.4	Past Simulation Results . . . . .	29

2.4	Benefits of a Deforming Blade . . . . .	31
2.5	Dynamic Mesh Methods . . . . .	31
2.5.1	Radial Basis Function Interpolations . . . . .	32
2.5.2	Linear Elasticity Equations . . . . .	33
2.5.3	Diffusion Smoothing . . . . .	33
2.5.4	Spring-Based Smoothing . . . . .	33
<b>3</b>	<b>Numerical Methods</b>	<b>35</b>
3.1	Governing Equations . . . . .	35
3.1.1	Ideal Gas Relations . . . . .	37
3.1.2	Pressure Calculation . . . . .	38
3.2	Large Eddy Simulations . . . . .	38
3.2.1	Subgrid Scale Models . . . . .	41
3.3	Discretization . . . . .	42
3.4	Time Step Size . . . . .	43
3.5	Meshing Considerations . . . . .	44
3.5.1	Domain Size . . . . .	44
3.5.2	Cell Size at the Wall . . . . .	44
3.6	Boundary Conditions . . . . .	44
3.6.1	Periodic Condition . . . . .	44
3.6.2	Walls . . . . .	45
3.6.3	Far-Field Condition . . . . .	45
3.6.4	Inflow . . . . .	45
3.7	Mesh Deformation . . . . .	45
3.7.1	Diffusion Smoothing . . . . .	46
3.7.2	Spring-Based Smoothing . . . . .	46
3.8	Force Calculations . . . . .	47

<b>4</b>	<b>LES Validation</b>	<b>48</b>
4.1	Experimental Comparison . . . . .	48
4.1.1	Experimental Setup . . . . .	48
4.1.2	WALE Simulation . . . . .	48
4.2	Laminar to Turbulent Transition . . . . .	49
<b>5</b>	<b>Oscillating Case</b>	<b>53</b>
5.1	Experimental Setup and Results . . . . .	53
5.2	Geometry . . . . .	55
5.3	Computational Domain . . . . .	55
5.4	Mesh . . . . .	55
5.5	Setup . . . . .	58
5.6	Oscillation Calculation . . . . .	58
5.7	Computational Time . . . . .	58
5.8	Convergence . . . . .	59
5.9	Results . . . . .	59
5.9.1	Aerodynamic Forces based on Angle of Attack . . . . .	62
<b>6</b>	<b>Deforming Case</b>	<b>66</b>
6.1	Geometry . . . . .	66
6.2	Computational Domain . . . . .	66
6.3	Mesh . . . . .	68
6.4	Setup . . . . .	71
6.5	Deformed Mesh Coordinates . . . . .	71
6.6	Convergence . . . . .	72
6.7	Results . . . . .	72
6.7.1	Aerodynamic Forces based on Time . . . . .	72
6.8	Deformation with Oscillation . . . . .	73

6.8.1 Oscillating a Deformed Airfoil . . . . .	75
<b>7 Conclusions and Future Work</b>	<b>79</b>

# List of Figures

1	the difference in global average temperature compared to the average temperature in 1951-1980 [20] . . . . .	13
2	the energy generation mix required to achieve energy transition by 2050 [35] . . . . .	14
3	left: horizontal axis wind turbines [24]; right: vertical axis wind turbine [33] . . . . .	15
4	a comparison of $C_P$ between a baseline, fixed profile, and deforming airfoil [55] . . . . .	18
5	VAWT motion and aerodynamic forces [43] . . . . .	21
6	a $C_P$ curve modified from [55] showing how the power coefficient changes as the turbine rotates . . . . .	22
7	comparing the $C_L - \alpha$ curve for an airfoil when it is quasi steady, versus when it is pitching [14] . . . . .	23
8	a drawing of the expected leading edge vortex roll-up, and images of the leading edge vortex roll-up from experiment [15] [23] . . . . .	24
9	a $C_L - \alpha$ curve demonstrating the effects of an increase in Reynolds number [14] . . . . .	25
10	a $C_L - \alpha$ curve demonstrating the effects of an increase in reduced frequency [14] . . . . .	26
11	the energy cascade [16] . . . . .	28

12	a $C_L - \alpha$ showing the results of LES simulations closely matching experimental data [28] . . . . .	30
13	the mesh around a flexing, rotating, and translating block at $t=0.25T$ and $t=0.75T$ [10] . . . . .	32
14	an extremely deformed aircraft wing accomplished using the linear elasticity equations [18] . . . . .	33
15	the spring method acts as though all of the nodes attached as tetrahedrals are connected via springs [39] . . . . .	34
16	Lift and drag curve slopes of a NACA0012 airfoil at a Reynolds number of 5,300, modified for readability from [44] . . . . .	49
17	comparing experimental results with WALE simulations . . . . .	50
18	the locations of where the velocity is being measured in time for the laminar to turbulent transition investigation . . . . .	51
19	changes in velocity with time during laminar to turbulent transition . . . . .	52
20	experimental results obtained using PIV by Choudhry et al. Starting at $0^\circ$ , each image is associated with a $5^\circ$ increase in angle of attack [14] . . . . .	54
21	a NACA0012 airfoil . . . . .	55
22	the computational domain with the airfoil at the center . . . . .	56
23	overall and close-up view of the computational mesh . . . . .	57
24	pressure contours showing the vortex growth visualized by the in-house LES code . . . . .	60
25	comparing the streamlines and the PIV images at $0^\circ$ and $10^\circ$ angle of attack . . . . .	61
26	comparing the streamlines and the PIV images at $20^\circ$ and $30^\circ$ angle of attack . . . . .	61

27	comparing the streamlines and the PIV images at 40° and 50° angle of attack . . . . .	62
28	the lift and drag coefficients with angle of attack for the oscillating airfoil	63
29	comparing the $C_L - \alpha$ curve for an airfoil when it is quasi steady, versus when it is pitching unsteadily [14] . . . . .	64
30	the $C_p$ curves for the oscillating airfoil . . . . .	65
31	the SSMA created by Pankonien et al. [51] . . . . .	67
32	the extremes of the deforming airfoil . . . . .	67
33	overall and close up views of the mesh for the deforming airfoil . . . .	68
34	the mesh around the airfoil when it has morphed completely upward .	69
35	the mesh around the tail when the airfoil is deformed completely upward	69
36	the mesh around the airfoil when it has morphed completely downward	70
37	the mesh around the tail when the airfoil is deformed completely downward . . . . .	71
38	pressure contours around the deforming airfoil . . . . .	73
39	streamlines around the deforming airfoil . . . . .	74
40	lift and drag coefficients with time for one cycle . . . . .	75
41	pressure coefficient with airfoil chord . . . . .	76
42	streamlines around an airfoil oscillated between 0 and 20 degrees . . .	77
43	comparing $C_p$ curves for the deformed airfoil and the NACA0012 . . .	78

# Nomenclature

## Acronyms

<i>CFD</i>	Computational fluid dynamics
<i>CFL</i>	Courant number
<i>DNS</i>	Direct numerical simulation
<i>GMRES</i>	Generalized minimum residual algorithm
<i>HAWT</i>	Horizontal axis wind turbine
<i>LES</i>	Large eddy simulation
<i>PIV</i>	Particle image velocimetry
<i>RANS</i>	Reynolds-averaged Navier Stokes
<i>RBF</i>	Radial basis function
<i>SGS</i>	Sub-grid scale
<i>SSMA</i>	Synergistic smart morphing aileron
<i>VAWT</i>	Vertical axis wind turbine
<i>WALE</i>	Wall adapting local eddy viscosity

## Coefficients and Constants

$C_D$	drag coefficient
$C_L$	lift coefficient

- $C_P$  power coefficient
- $C_p$  pressure coefficient, specific heat
- $C_S$  Smagorinsky constant
- $C_w$  WALE constant

## Math

- $div$  divergence
- $\Delta$  derivative
- $\delta$  partial derivative
- $\delta_{ij}$  Kronecker delta
- $G()$  convolution filter
- $\Sigma$  sum
- $\bar{\bullet}$  filtered part of a variable
- $\tilde{\bullet}$  Favre filtered part of a variable
- $\bullet'$  sub-grid part of a filtered variable
- $\bullet''$  sub-grid part of a Favre filtered variable
- $\vec{\bullet}$  vector

## Non-Dimensional Numbers

- $\gamma$  ratio of specific heats
- $Pr$  Prandtl number
- $Re$  Reynolds number
- $y+$  dimensionless wall distance

## Symbols

$A$	area	$[m^2]$
$c$	chord	$[m]$
$d_{ij}$	distance between i and j	$[m]$
$e$	internal energy	$[J]$
$E_T$	total energy	$[J]$
$F$	force	$[N]$
$F_D$	drag force per unit length	$[N/m]$
$F_L$	lift force per unit length	$[N/m]$
$F_T$	tangential force per unit length	$[N/m]$
$k$	spring stiffness	$[N/m]$
$p$	pressure	$[Pa]$
$q_j$	heat flux	$[W/m^2]$
$Q_j$	sub-grid scale temperature flux	$[W/m^2]$
$R$	gas constant	$[J/mol]$
$S$	surface area	$[m^2]$
$S_{ij}$	shear rate tensor	$[m/s]$
$u^*$	friction velocity	$[m/s]$
$t$	instantaneous time	$[s]$
$T$	total time, temperature	$[s], [K]$
$u$	velocity in the x direction	$[m/s]$
$v$	velocity in the y direction	$[m/s]$
$w$	velocity in the z direction	$[m/s]$
$\alpha$	angle of attack in degrees	$[^\circ]$
$\Delta$	filter size	$[m^2]$
$\gamma$	diffusion constant	$[1/m]$

$\kappa$	thermal conductivity	$[\frac{W}{mK}]$
$\mu$	dynamic viscosity	$[Pa \cdot s]$
$\nu$	kinematic viscosity	$[m^2/s]$
$\Omega$	domain size	$[m^2]$
$\Omega_{mn}$	vorticity	$[m/s]$
$\rho$	density	$[kg/m^3]$
$\sigma$	shear-stress tensor	$[Pa]$
$\tau$	stress term	$[Pa]$

# Chapter 1

## Introduction

### 1.1 Overview

The globe is warming quickly: between 1906 and 2005, the globe's average surface temperature has increased by  $0.74 \pm 0.18^\circ\text{C}$  [8]. NASA, which has been measuring the surface temperature of the earth since 1880, has shown the upward trend of global temperature by plotting the global mean temperature anomaly based on land and ocean data, as seen in Figure 1 [20].

This warming is caused by the release of greenhouse gases, which trap heat and warm the atmosphere. These gases are released primarily by human activities; most significantly, power generation [4].

The impacts of global warming will be devastating for humanity [4]. These impacts may include but are not limited to, the spread of infectious diseases, flooding of cities and agricultural lands, species extinction, reduction in crop yields, and an increase in global poverty [4]. As a result, governments are reducing their reliance on carbon producing sources of energy and transitioning to renewable sources.

Wind power is a well-established and globally supported source of renewable energy [29]. Though a mix of renewable energy sources is required due to the wind's

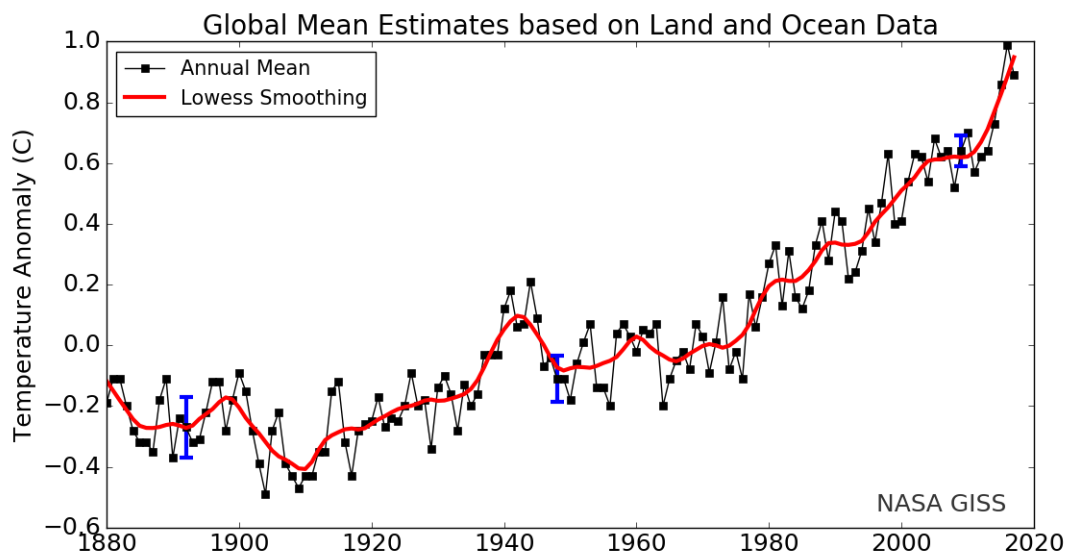


Figure 1: the difference in global average temperature compared to the average temperature in 1951-1980 [20]

inherit inconsistencies, wind energy plays a significant part in the global energy transition [35]. Figure 2 shows the breakdown of renewable sources that the International Renewable Energy Agency believes is required to achieve energy transition by 2050 [35].

### 1.1.1 Wind Energy Today

In 2016, Canada had the capacity to produce 11.7 GW of energy from wind [9]. This number is expected to grow continuously until 2038 when the National Energy Board predicts the country will have an installed capacity of 19.4 GW [9]. The majority of these wind turbines are tall, with three blades turning like a pinwheel, producing power as part of a wind farm.

Wind turbines like these are classified as horizontal axis wind turbines (HAWTs). This classification is based on the relationship between the turbine’s axis of rotation and the direction of the incoming flow [40]. For HAWTs, the axis of rotation is parallel to the flow [40]. Available alongside HAWTs are vertical axis wind turbines

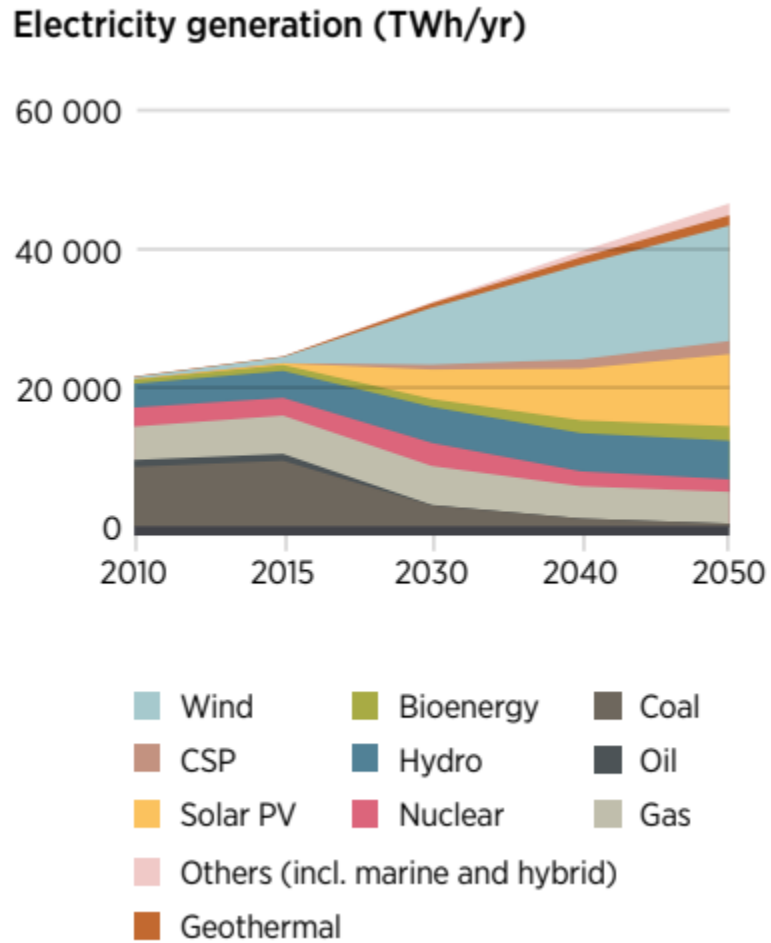


Figure 2: the energy generation mix required to achieve energy transition by 2050 [35]



Figure 3: left: horizontal axis wind turbines [24]; right: vertical axis wind turbine [33]

(VAWTs), which have an axis of rotation perpendicular to the flow [40]. Figure 3 provides an image of both for comparison.

In the 1980s, the European renewable energy industry decided that wind turbine research and development should focus on HAWTs, because their pitch control systems and wake development were simpler than those in VAWTs, and their ability to be built at high altitudes would allow them to capture higher wind speeds [53]. As a result of three decades of research, HAWTs are well-developed and frequently used, with better power production than VAWTs.

However, HAWTs are not the best turbine for every application. VAWTs can capture wind flowing from any direction, in contrast to HAWTs, which are highly directional; and VAWTs are also easier to maintain because their gearboxes are located closer to the ground [40]. VAWTs are thus potentially a better choice for microgrids and urban applications.

Even though VAWTs are slowly gaining visibility, due to the comparative lack of research, VAWTs frequently do not produce enough power to be an economical investment. One way to improve VAWTS would be to use a blade designed for the

complex aerodynamics VAWTs experience. This thesis analyzes a tool that can be used to model the aerodynamic forces on a VAWT blade, so these blades can be better analyzed and designed.

### **1.1.2 VAWT Aerodynamic Considerations**

Understanding the aerodynamics of a wind turbine design is vital for predicting the forces acting on the blades, which in turn affect the turbine's power output. VAWTs have complicated flow patterns, which includes the formation of the dynamic stall vortex.

Dynamic stall occurs when a blade is pitching unsteadily [26]. In addition to its appearance over wind turbine blades, it can also be seen over helicopter blades and during the flapping of micro aerial vehicle wings [26]. It leads to a delay in flow separation, meaning the vortex on the suction side of the airfoil remains longer than it would in a static case. This vortex increases the lift force, and thus the power production, of the blade while it is present. Alongside other aerodynamic considerations, dynamic stall needs to be studied to improve VAWT power production.

### **1.1.3 Simulations of VAWT Aerodynamics**

Performing a wind tunnel experiment every time dynamic stall needs to be observed or its forces measured is not a cost-effective suggestion. Thus, a numerical model needs to be used to be able to understand the flow structures present. In this thesis, computational fluid dynamics (CFD) is used. The CFD community has not yet reached a consensus about how the growth and convection of the dynamic stall vortex should be modeled.

CFD simulations are often done using Reynolds-Averaged Navier Stokes (RANS) models. RANS models are popular since they are trusted in commercial software, their use has been documented extensively, and they are relatively inexpensive for CFD.

However, since the turbulence is modeled and not solved, these codes can have issues with accuracy. The most accurate way to perform CFD would be direct numerical simulations (DNS), but DNS is too expensive for today's computing resources.

The option in between RANS models and DNS is large eddy simulations (LES). LES calculates the eddy viscosity of eddies larger than a filter size and models the rest. This provides a picture of the flow with most of the accuracy of DNS, but without its computational expense. LES will be used to perform the aerodynamic analysis that will be presented in this thesis.

### 1.1.4 Potential Improvements

As will be shown in the literature review in Chapter 2, being able to maintain the vortex over the blade would increase the lift and the power production. At the University of Michigan, researchers have developed a deforming airfoil with a morphing tail that could be used to hold the vortex in place [51]. The blade is called a Synergistic Smart Morphing Aileron (SSMA) [51]. It combines shape memory wire actuators and macro-fiber composites, two components that are often employed alone, but which suffer from slow response times and limited actuation strains, respectively [51]. The combination of the two allows for the large deflections that are characteristic of shape memory alloys, as well as the control provided by the macro-fiber composites [51]. Using this morphing blade creates a higher power coefficient,  $C_P$ , curve with azimuth angle, compared to a fixed profile [55].  $C_P$  curves with azimuth angle for a VAWT using the deforming airfoil can be seen in Figure 4.

## 1.2 Contributions

In this thesis, the dynamic stall vortex structures that appear over an oscillating NACA0012 airfoil, and the aerodynamic structures over the deforming SSMA are

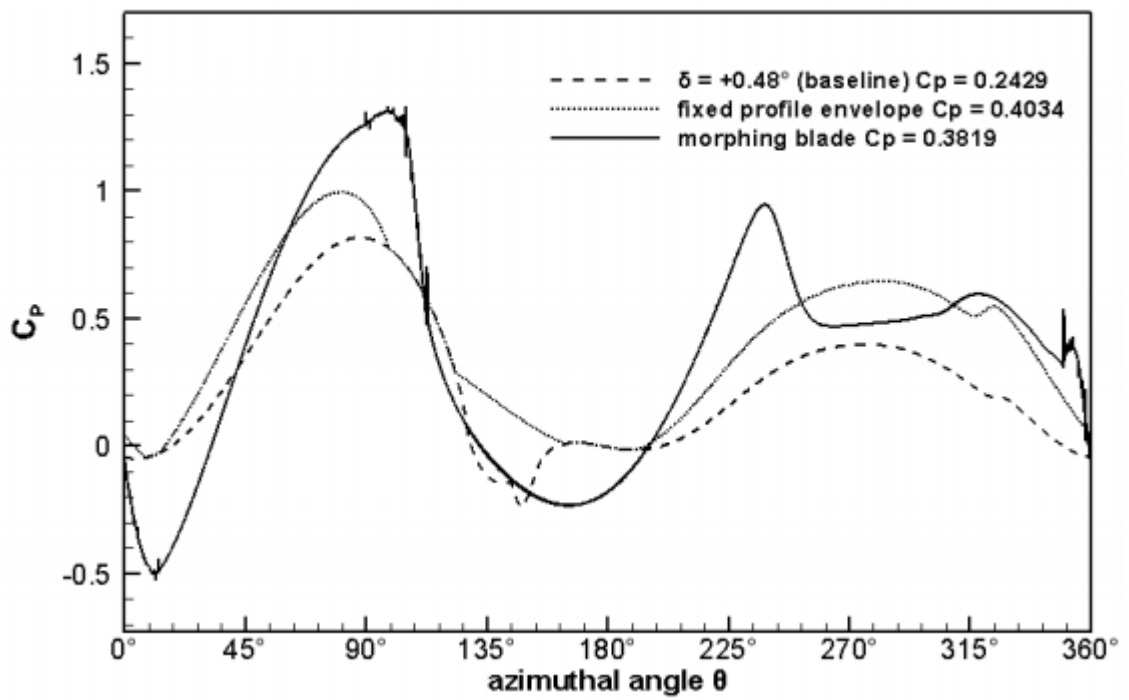


Figure 4: a comparison of  $C_p$  between a baseline, fixed profile, and deforming airfoil [55]

simulated using LES. In-house code captures the main features of the dynamic stall vortex, showing that LES can be used to study complex, unsteady flows, and is able to deform the computational mesh.

## 1.3 Thesis Contents

The remainder of this thesis will be laid out as follows.

First, a review of relevant theory and literature will be provided in Chapter 2. This includes a more in-depth explanation of dynamic stall, CFD simulations including dynamic meshes, and the benefits of a deforming blade.

Chapter 3 provides an overview of the numerical methods that are used in the CFD code, including the governing equations, discretization methods, boundary conditions and time step size.

Chapter 4 compares an experimental lift curve slope with one simulated with by code and shows the ability of the in-house code to simulate laminar to turbulent transition.

Chapter 5 gives details of the simulation setup, the results of a case compared to an experiment, for the oscillating airfoil case. Pressure contours of the LES results are shown next to experimental PIV images, and the force coefficients are presented with angle of attack.

Chapter 6 provides details of the deforming airfoil's simulation setup and the results of the simulation for analysis. The results include pressure contours, graphs of force coefficients with time, and graphs of the coefficient of pressure with the chord. The deformed airfoil is then oscillated, showing the ability of the in-house code to pick up vortices in the flow.

The results are discussed and summarized in Chapter 7.

# Chapter 2

## Theory and Literature Review

### 2.1 Effects of Airfoil Aerodynamics on VAWT Power Production

Wind turbines extract power from the wind by using the aerodynamic forces acting on the blades to create a moment about the axis of rotation [1]. This moment is the torque applied to a generator shaft, which can then create electricity [2].

The aerodynamic forces are generated by the flow passing over an airfoil, which has a geometry that creates a pressure difference between its upper and lower surfaces [1]. This pressure difference results in the creation of the lift and drag forces [1]. The geometry used in these calculations can be seen in Figure 5.

The tangential force is required to calculate the torque [55]. The tangential force is based on the lift and drag, and its equation is as follows:

$$F_T = F_L \sin \phi - F_D \cos \phi \quad (1)$$

where  $F_T$  is the tangential force,  $F_L$  is the lift force,  $\phi$  is the angle of the resultant flow velocity, and  $F_D$  is the drag force. To find the torque applied to the generator shaft, the tangential force simply has to be multiplied by the distance of the blade to

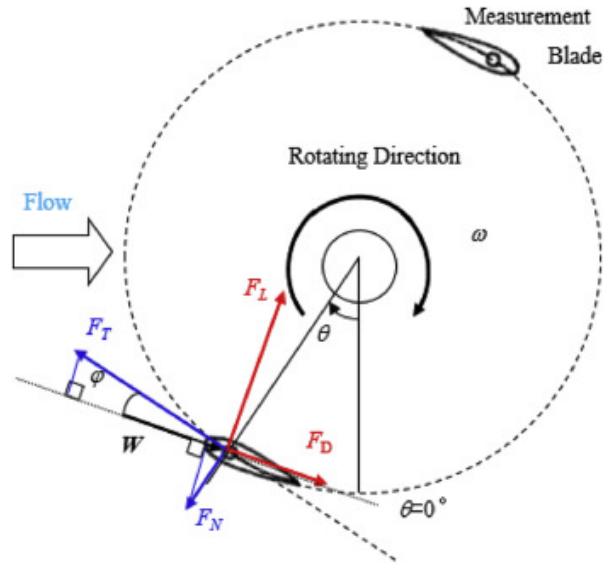


Figure 5: VAWT motion and aerodynamic forces [43]

the shaft [55].

Figure 6 shows how the power coefficient of an airfoil changes with its azimuth position. The highest power corresponds to the time right before the airfoil goes into dynamic stall. Stall occurring earlier would thus reduce the  $C_P$  that the VAWT could achieve.

## 2.2 Static Versus Dynamic Stall

Stall is the catastrophic loss of lift that occurs when a boundary layer separates from a surface due to an adverse pressure gradient [49]. If stall is static, this means that it occurred over a surface which was remaining at a single angle of attack.

Airfoils have  $C_L - \alpha$  curves that show how, after a specific angle of attack, the lift coefficient for the airfoil dramatically drops off [5]. The angle at which this occurs is the stall angle [5]. If stall is dynamic, the airfoil is pitching when the catastrophic loss of lift occurs [27].

Static and dynamic stall have different characteristics. During dynamic stall, separation is delayed until a higher angle of attack. An airfoil undergoing dynamic

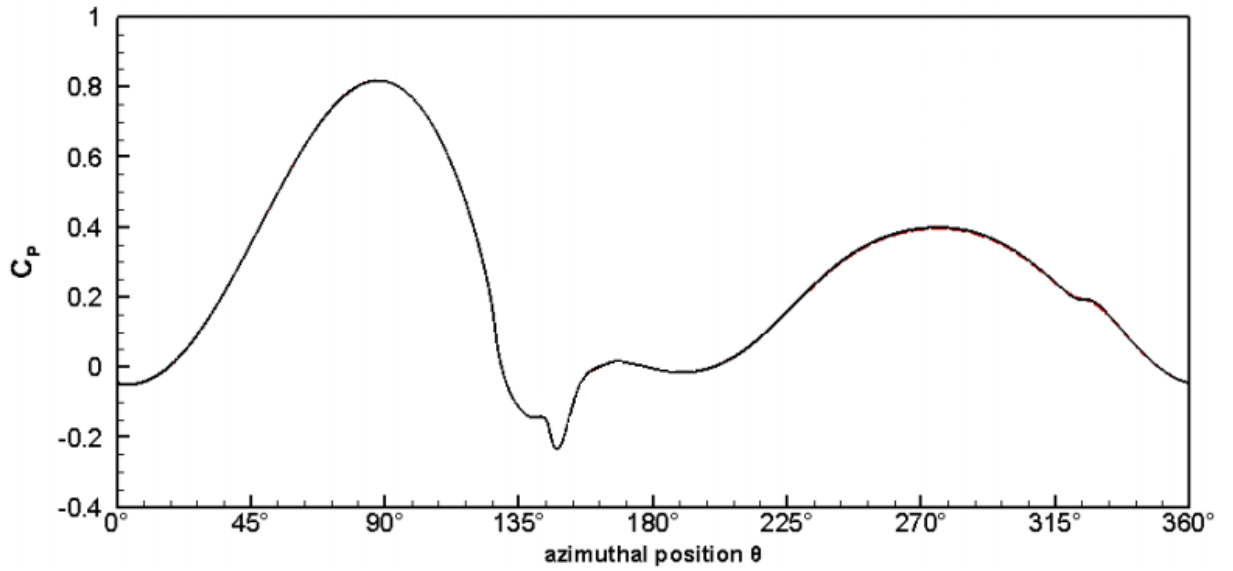


Figure 6: a  $C_P$  curve modified from [55] showing how the power coefficient changes as the turbine rotates

stall also experiences higher lift overall. The difference in their  $C_L - \alpha$  curves can be seen in the Figure 7.

While both static and dynamic stall ultimately lead to a catastrophic loss of lift, the dynamic stall process is more complicated than a simple flow separation. The following sections will provide a brief description of what occurs during dynamic stall, and the properties that cause these effects.

### 2.2.1 The Dynamic Stall Process

Dynamic stall was discovered as an aspect of unsteady flow. Initially, it was believed to be caused by a bursting laminar separation bubble [46]. Wind tunnel experiments by McCroskey et al. showed that it was instead caused by a breakdown of the turbulent boundary layer [46].

That conclusion has been confirmed through additional in-depth experiments, such as the work of Mulleners et al., who used surface measurements and particle image velocimetry (PIV) to study the dynamic stall process, and Lee et al., who

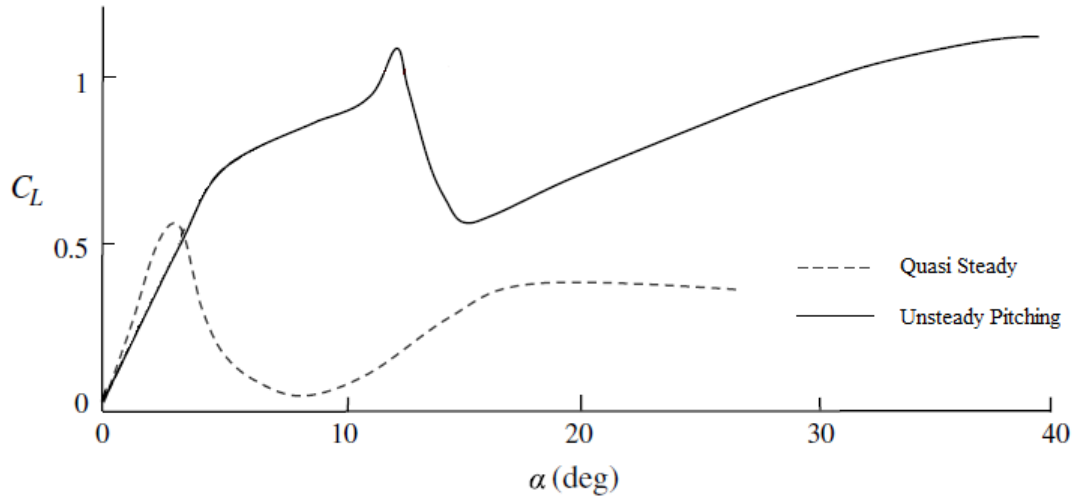


Figure 7: comparing the  $C_L - \alpha$  curve for an airfoil when it is quasi steady, versus when it is pitching [14]

studied dynamic stall using hot-film sensor arrays [48] [41]. Both studied oscillating NACA0012 airfoils [48] [41].

After an airfoil pitches past its static stall angle of attack, recirculation begins to occur above its surface [48]. A shear layer grows between the reversed flow and the free stream, which contains multiple, evenly spaced vortices [48]. The vortices then begin to interact and merge, leading the shear layer to roll up into the dynamic stall vortex [48]. This separation bubble is shorter than one seen in the static stall case [41]. The dynamic stall vortex remains until it detaches and is carried away by the freestream, which causes the loss of lift associated with stall [48]. The flow later rejoins the leading edge during the airfoils downstroke [48]. Figure 8 shows the roll-up drawn by Corcos et al., and the PIV images captured by Fujisawa et al.

Dynamic stall over a VAWT can cause structural fatigue that can lead to failure [3]. In many cases, the stresses caused by dynamic stall are the limiting factor on VAWT performance and structure [3].



Figure 8: a drawing of the expected leading edge vortex roll-up, and images of the leading edge vortex roll-up from experiment [15] [23]

## 2.2.2 Factors Affecting the Dynamic Stall Process

Many factors have been experimentally shown to affect the dynamic stall process. The four that relate directly to the simulations that will be performed for this thesis will be discussed below.

### Type of Motion

The unsteady flow over airfoils is affected by airfoil's type of motion [45]. Airfoils can move in the roll, pitch, and yaw directions, and can experience plunging, gusts, step changes, and cascades [45]. These types of motion affect flow interactions and pressure distributions [45].

### Airfoil Shape Effects

The shape of an airfoil is known to affect its lift and stall characteristics, due to the potential of an airfoils shape to alter the suction sides pressure distribution [52]. Airfoil shape can also determine the location along the chord that flow separation occurs [52]. This can prevent or delay the formation of the dynamic stall vortex [37].

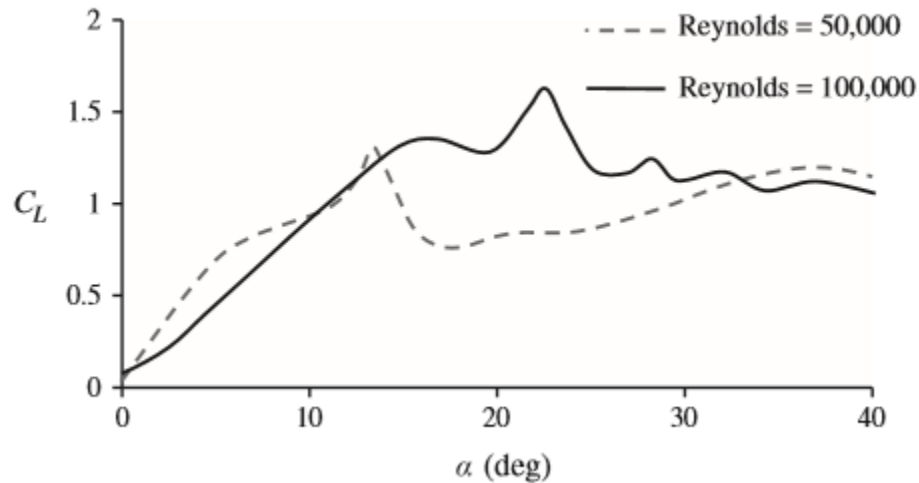


Figure 9: a  $C_L - \alpha$  curve demonstrating the effects of an increase in Reynolds number [14]

### Reynolds Number Effects

Figure 9 from “An insight into the dynamic stall lift characteristics” from Choudhry et al. shows the effects of increasing the Reynolds number on an airfoil undergoing dynamic stall [14]. Increasing the Reynolds number delays the detachment of the dynamic stall vortex since the higher Reynolds number flows force the flow to remain attached and have a more difficult time separating from the suction side of the airfoil [14].

This phenomenon is not seen in high Reynolds number flows, because these flows lower the viscosity sufficiently to allow the generation of small-scale turbulence [61]. Small-scale turbulence affects the integrity of the dynamic stall vortex [61].

### Reduced Frequency Effects

Reduced frequency is a dimensionless number used to study the unsteadiness of a flow by describing how an object vibrates when a flow moves past it [21]. Its value is based on the blades rotational frequency and chord, and the velocity of the freestream

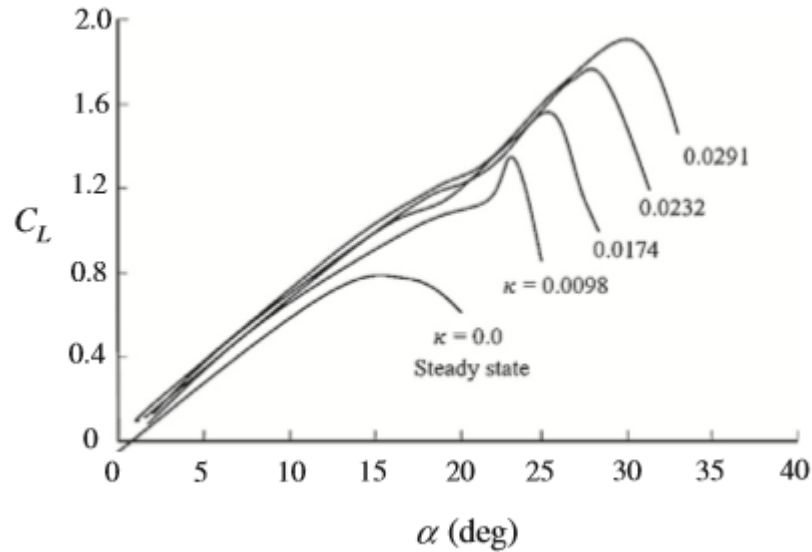


Figure 10: a  $C_L - \alpha$  curve demonstrating the effects of an increase in reduced frequency [14]

[21]. Choudhry et al. observed that the maximum achievable coefficient of lift of an airfoil undergoing dynamic stall increases as reduced frequency increases [14]. This is because the reduced frequency slows the transition point's forward motion along the airfoil so that the turbulent boundary layer can resist flow reversal [41].

### 2.2.3 Mach Number Effects

A study performed by Carr et al. showed that the Mach number of a flow affects its dynamic stall behaviours [13]. These compressibility effects begin at a Mach number of 0.2 and include changes in the dynamic stall vortex development and the lift overshoot [13].

## 2.3 Dynamic Stall Simulation

Compared to performing wind tunnel experiments, numerical methods and CFD simulations are a time- and cost-saving way to understand the physics of a fluid flow.

### 2.3.1 Numerical Methods

Carr presented an initial overview of dynamic stall models in 1988 [12]. Many of the initial numerical models were based on the Navier-Stokes equations, and provided a good correlation with experimental results for specific cases [12]. Others were semi-empirical, such as the still-popular model introduced by Leishman et al. in 1986 [42]. However, early numerical methods could not model low-Reynolds transitional flows [19]. This required the introduction of turbulence models, and led to the emergence of RANS models [19].

### 2.3.2 RANS Models

The RANS equations describe fluid flow by decomposing the Navier Stokes equations into time-averaged and fluctuating portions. These equations are closed with turbulence models to describe the flow viscosity. Using models to close the RANS equations can be beneficial because they are the simplest, and thus the least expensive, method for simulating a turbulent flow.

The most popular models, such as Spalart Allmaras and  $k-\epsilon$ , are known to produce good results in certain situations [7]. However, they suffer from a lack of accuracy in many conditions of interest to the present study - specifically, in the accurate modeling of diffusion and the adverse pressure gradients related to the roll-up of the leading edge vortex [7]. Since RANS models are averages, they often miss the unsteadiness inherent to the physics of fluid flow [22].

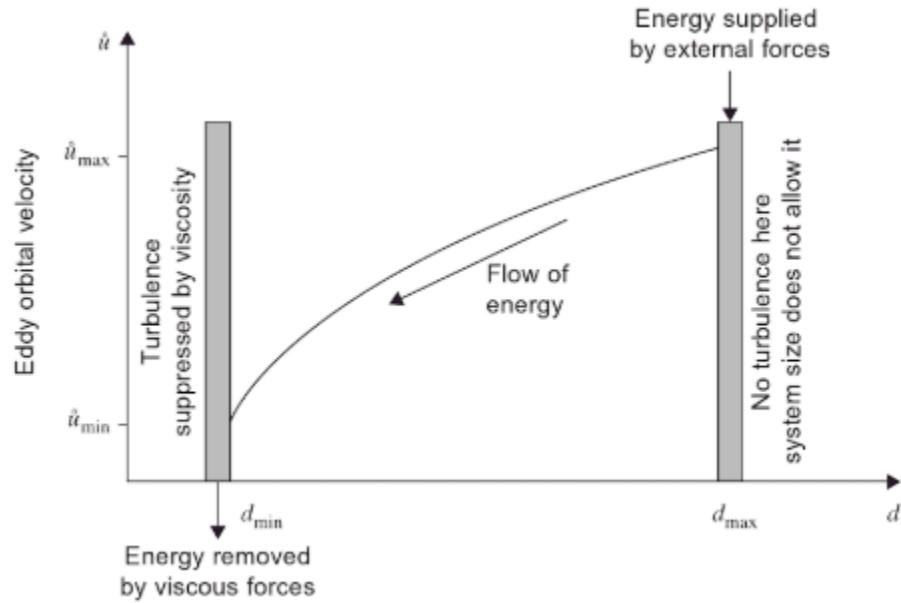


Figure 11: the energy cascade [16]

### 2.3.3 Large Eddy Simulation

Large eddy simulations are closer to direct numerical solutions than RANS models since they only model the smallest energy contributors to the flow.

The principle of large eddy simulations is based on the Kolmogorov length scales. Kolmogorov states that there is a wide range of sizes of turbulent motions, the largest being the ones created by energy provided by external forces, all the way down to the smallest eddies, which are eventually dissipated by viscosity [38]. This is demonstrated by the image of the energy cascade, shown in Figure 11. The larger the eddy, the more significant its energy contribution to the flow.

Large eddy simulations only consider eddies that make a significant energy contribution. A high-pass scale filter allows the code to ignore any eddies smaller than the size of the grid [39].

In the in-house code, a box filter is applied to remove small eddies. The size of the smallest cell is defined by the  $y+$  value of the mesh. The  $y+$  value is defined as:

$$y^+ = \frac{u^* y}{\nu} \quad (2)$$

where  $y$  is the distance from the wall,  $\nu$  is the kinematic viscosity, and  $u^*$ , the friction velocity, is defined as:

$$u^* = \sqrt{\frac{\tau_w}{\rho}} \quad (3)$$

Setting the  $y^+$  value of the first cell of the wall to be less than one allows the center of the cell to be located inside the viscous sublayer. This allows the boundary layer to be fully resolved, leading to high-quality results.

For flow that occurs inside the confines of the box filter, subgrid-scale models are used. Subgrid-scale eddies are more straightforward to model than large eddies, as the smallest eddies are more often isotropic and homogeneous [62].

While it is more accurate than RANS simulation, LES is not always used because of its high computational costs.

### 2.3.4 Past Simulation Results

RANS models have been used extensively to model dynamic stall around oscillating airfoils undergoing dynamic stall. Some examples include the simulations performed by Buchner et al., Hand et al., and Tseng et al. [11] [31] [56]. Each of these groups produced results sufficient in some applications but observed some discrepancies [11] [31] [56]. Hand et al. and Tseng et al. suggested eddy simulations be used instead if the computational resources are available [31] [56].

LES has been used less often because it is more computationally expensive. Validation results available show good agreement between experiment and LES below the stall angle, as can be seen in the results provided by Gillaud et al. in Figure 12 [28]. Experiments performed by Wang et al. showed a similarly good agreement for the lift coefficient values when the angle of attack was below stall, but above stall,

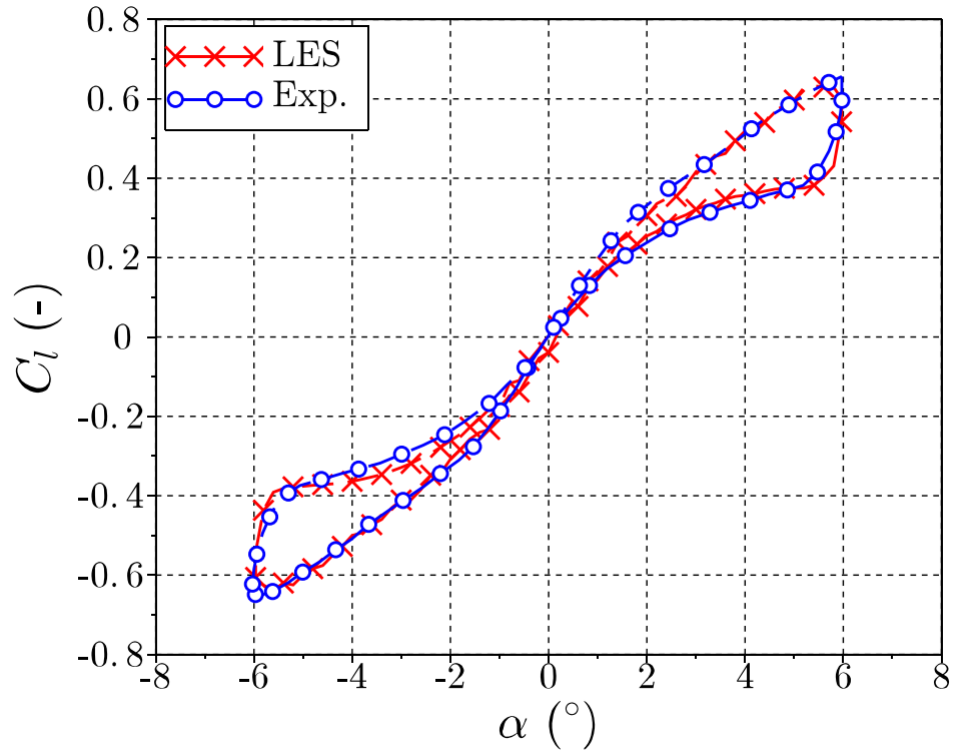


Figure 12: a  $C_L - \alpha$  showing the results of LES simulations closely matching experimental data [28]

LES overestimated the lift [58]. Both above and below stall, the drag coefficient was too high [58]. However, Wang et al. were using a CFD code developed by the Wind Energy Institute at the Technical University of Denmark, which has been seen to produce poor results when LES turbulence modeling is used [30].

It can therefore be seen in the literature that while RANS models can provide good results, these results often contain inaccuracies. While their use is understandable, with access to high-performance computers, LES simulations can be done relatively quickly with superior results.

No matter the turbulence models used, the literature suggests the use of fully 3D models where possible. Fully 3D models produce better results hysteresis loops than models in 2D [60]. 2D and 2.5D models also cannot show the influence of three-dimensional effects over the airfoil [60]. The 3D effects are significant, especially at

high angles of attack and during the down-stroke [59]. In 2005, RANS experiments comparing 2D and 3D simulations to experimental data, and determined that the 2D results were only useful in the midspan location [54].

## 2.4 Benefits of a Deforming Blade

The idea behind a deforming blade is the shape of an airfoil can control separation and thus control stall [52] [37]. For this study, a deforming blade could hold the dynamic stall vortex in place by blocking its normal convection path. Since it is the dynamic stall vortex being carried away by the free stream that leads to the loss of lift that is stall, the idea is that a deforming blade would allow the lift to continue to grow at even higher angles of attack.

Using a deforming blade to delay stall and increase lift has been done successfully by many researchers. At the 2014 Asia-Pacific International Symposium on Aerospace Technology, Hefeng et al. showed that airfoils with flexible structures have better lift coefficients than their rigid counterparts because the flexibility of the airfoils reduced the separation of the flow [32]. Similarly, Jones et al. saw an increase in lift and a decrease in drag at all tested angles of attack, when a periodic surface motion was added to a NACA4415 using Macro Fiber Composites [36]. Tan demonstrated that the stall of a deforming blade is delayed compared to an airfoil with a fixed profile [55].

## 2.5 Dynamic Mesh Methods

There are several methods for working with a dynamic mesh. When a body is deforming, the code must either re-create the mesh at each iteration to account for the new geometry or move each of the vertices without affecting the connections between cells [39].

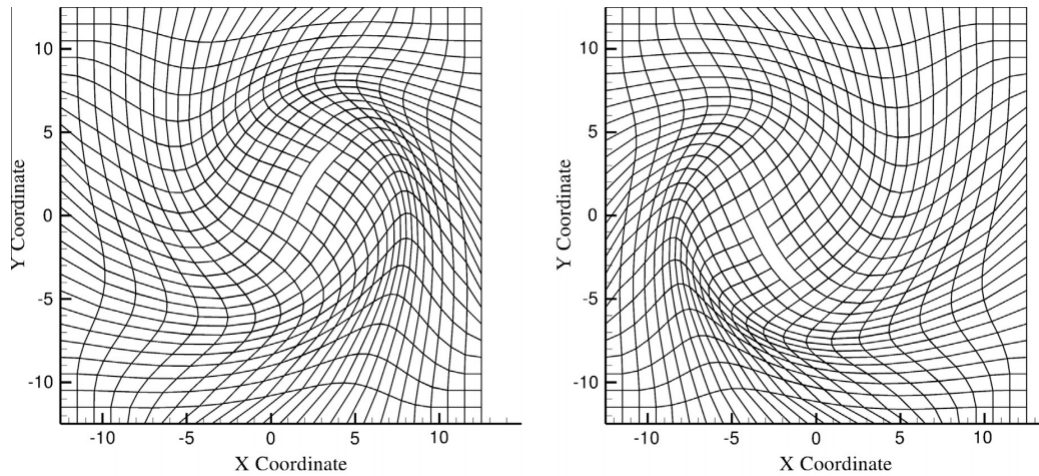


Figure 13: the mesh around a flexing, rotating, and translating block at  $t=0.25T$  and  $t=0.75T$  [10]

Though remeshing is popular and is used by commercial software such as ANSYS FLUENT, it is not applicable to cases done with parallel computing, as remeshing changes the connectivity of the cells [6]. The in-house code does not account for any changes in connectivity; thus remeshing cannot be used for these simulations [39]. The more popular of the remaining options are described below.

### 2.5.1 Radial Basis Function Interpolations

Radial basis function (RBF) interpolation, created by de Boer et al., calculates the displacement of internal fluid nodes based on the displacement of the nodes on the surface body [17]. Bos et al. found that using RBF interpolation to deform the mesh around a flapping wind provided results in a high-quality mesh, with a low amount of skewness compared to Laplace-based smoothing methods [10]. Examples of their results can be seen in Figure 13.

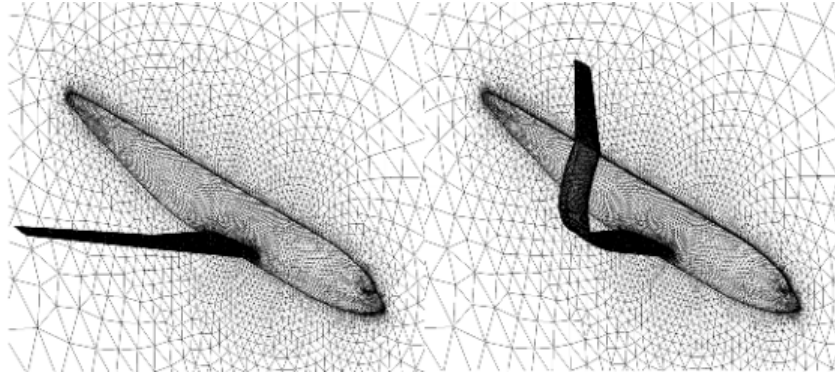


Figure 14: an extremely deformed aircraft wing accomplished using the linear elasticity equations [18]

### 2.5.2 Linear Elasticity Equations

Mesh deformation can be achieved by treating the deforming mesh as a deforming, elastic solid [18]. If the deformation is applied to the mesh incrementally, using the linear elasticity equations allows for extreme deformation, such as the deformation of a whole aircraft wing seen in Figure 14 [18].

### 2.5.3 Diffusion Smoothing

Diffusion smoothing is also known as Laplacian smoothing [6]. It is the simplest and most inexpensive smoothing method [6]. The diffusion smoothing method solves the Laplace equation and can be controlled by either cell volume, or the distance from a cell to the wall [39]. In either case, if a cell is close to the wall, it experiences higher diffusion and therefore moves more quickly than a cell far from the wall [39].

### 2.5.4 Spring-Based Smoothing

In the spring method, Hooke's law is applied at each grid point [6]. The new coordinates of each vertex are calculated using linear extrapolation and iterative methods [39]. Figure 15 shows how all of the vertices of a tetrahedral are connected.

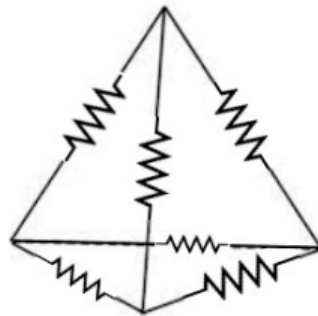


Figure 15: the spring method acts as though all of the nodes attached as tetrahedrals are connected via springs [39]

# Chapter 3

## Numerical Methods

This chapter presents the governing equations, the discretization method, an overview of large eddy simulations, and the method used to calculate the forces on the blades.

### 3.1 Governing Equations

The goal of a CFD simulation is to provide a solution of a flow, over an entire domain, through a period of time. Several equations are required to describe the velocity, pressure, density, and temperature of a fluid.

Compressible versions of equations are used in the in-house code to improve its robustness [39]. In cases where the Mach number is low, such as the cases presented in this thesis, a preconditioner needs to be used [39]. The preconditioner is implemented as per the method described by Viozat's 1997 thesis, "Implicit upwind schemes for low Mach number compressible flows" [57].

#### Continuity Equation

The continuity equation is an expression of the conservation of mass. The continuity equation for fluids is:

$$\frac{\partial \rho}{\partial t} + \frac{\partial (\rho u)}{\partial x} + \frac{\partial (\rho v)}{\partial y} + \frac{\partial (\rho w)}{\partial z} = 0 \quad (4)$$

where  $\rho$  is the fluid density,  $t$  is the time, and  $u$ ,  $v$ , and  $w$  are the velocities in the  $x$ ,  $y$ , and  $z$  directions. This equation captures the changing density due to compressible flow.

## Conservation of Momentum

The conservation of momentum equations are an expression of how, in a closed system, the total amount of linear momentum must remain constant.

The momentum of an object depends on its mass and velocity. Any change in momentum means a force is being exerted. These simple statements can be used to describe a fluid flow by relating the mass to the fluid's density, and defining the force using its two components - forces due to stress created by the viscosity of the fluid, and body forces.

The conservation of momentum equations are:

$$\frac{\partial (\rho u)}{\partial t} + \frac{\partial (\rho u^2)}{\partial x} + \frac{\partial (\rho uv)}{\partial y} + \frac{\partial (\rho uw)}{\partial z} = -\frac{\partial p}{\partial x} + \frac{1}{Re} \left[ \frac{\partial \tau_{xx}}{\partial x} + \frac{\partial \tau_{xy}}{\partial y} + \frac{\partial \tau_{xz}}{\partial z} \right] \quad (5)$$

$$\frac{\partial (\rho v)}{\partial t} + \frac{\partial (\rho uv)}{\partial x} + \frac{\partial (\rho v^2)}{\partial y} + \frac{\partial (\rho vw)}{\partial z} = -\frac{\partial p}{\partial y} + \frac{1}{Re} \left[ \frac{\partial \tau_{xy}}{\partial x} + \frac{\partial \tau_{yy}}{\partial y} + \frac{\partial \tau_{yz}}{\partial z} \right] \quad (6)$$

$$\frac{\partial (\rho w)}{\partial t} + \frac{\partial (\rho uw)}{\partial x} + \frac{\partial (\rho vw)}{\partial y} + \frac{\partial (\rho w^2)}{\partial z} = -\frac{\partial p}{\partial z} + \frac{1}{Re} \left[ \frac{\partial \tau_{xz}}{\partial x} + \frac{\partial \tau_{yz}}{\partial y} + \frac{\partial \tau_{zz}}{\partial z} \right] \quad (7)$$

where  $p$  is the pressure,  $Re$  is the Reynolds number, and the  $\tau$  are the stress terms. The left-hand side of these equations are convection terms, while the stresses on the right multiplied by the inverse of the Reynolds number are the diffusion terms. Since the diffusion terms are related to the stresses created by viscosity, they are the terms related to turbulence and boundary layer generation.

## Conservation of Energy

The conservation of energy equation in fluids is an expression of how, in a closed system, energy cannot be created or destroyed, only transformed. The conservation of energy equations are:

$$\begin{aligned} \frac{\partial (E_T)}{\partial t} + \frac{\partial (uE_T)}{\partial x} + \frac{\partial (vE_T)}{\partial y} + \frac{\partial (wE_T)}{\partial z} = & \\ & - \frac{\partial (up)}{\partial x} - \frac{\partial (vp)}{\partial y} - \frac{\partial (wp)}{\partial z} - \frac{1}{RePr} \left[ \frac{\partial (q_x)}{\partial x} + \frac{\partial (q_y)}{\partial y} + \frac{\partial (q_z)}{\partial z} \right] \\ + \frac{1}{Re} \left[ \frac{\partial}{\partial x} (u\tau_{xx} + v\tau_{xy} + w\tau_{xz}) + \frac{\partial}{\partial y} (u\tau_{xy} + v\tau_{yy} + w\tau_{yz}) + \frac{\partial}{\partial z} (u\tau_{xz} + v\tau_{yz} + w\tau_{zz}) \right] & \end{aligned} \quad (8)$$

where  $E_T$  is the total energy,  $Pr$  is the Prandtl number, and  $q$  is the heat flux. This equation contains the temperature of the fluid inside the total energy term.

### 3.1.1 Ideal Gas Relations

Since the code requires the density in many locations, it needs to be solved for using the pressure and the temperature of the fluid. In the in-house code, it is the ideal gas law that is used to calculate the density. The ideal gas law is:

$$p = \rho RT \quad (9)$$

where  $R$  is the gas constant and  $T$  is the temperature. The ideal gas equation is also used in energy calculations. For ideal gases, the internal energy is a function of temperature, exclusively. The total energy including pressure and kinetic energy is:

$$\rho e = \frac{p}{(\gamma - 1)} + \frac{1}{2} \rho u_i^2 \quad (10)$$

where  $e$  is the internal energy and  $\gamma$  is the ratio of specific heats.

### 3.1.2 Pressure Calculation

The pressure is calculated from the total energy per unit mass:

$$E_T = \frac{1}{2}u^2 + e \quad (11)$$

The equation is closed using the expression for the internal energy per unit mass for a polytropic gas [39]:

$$e = \frac{p}{(\gamma - 1)\rho} \quad (12)$$

## 3.2 Large Eddy Simulations

LES separates the flow based on the flow scale. This is done by filtering the governing equations and solving the flow that is captured by the mesh while modeling the smallest eddies.

To use the filters, the governing equations for LES need to be expressed in their conservation forms [25]:

$$\frac{\partial \rho}{\partial t} + \frac{\partial (\rho u_j)}{\partial x_j} = 0 \quad (13)$$

$$\frac{\partial (\rho u_i)}{\partial t} + \frac{\partial (\rho u_i u_j)}{\partial x_j} + \frac{\partial p}{\partial x_i} = \frac{\partial \sigma_{ij}}{\partial x_j} \quad (14)$$

$$\frac{\partial (E_T)}{\partial t} + \frac{\partial (\rho E_T + p) u_j}{\partial x_j} = \frac{\partial \sigma_{ij} u_i}{\partial x_j} - \frac{\partial}{\partial x_j} q_j \quad (15)$$

where  $x_i$  represents the location in on a Cartesian coordinate system,  $u_i$  represents the three components of velocity, and  $q_j$  represents the heat flux [25].

The shear-stress tensor can be rewritten as [25]:

$$\sigma_{ij} = 2\mu T S_{ij} - \frac{2}{3}\mu T \delta_{ij} S_{kk} \quad (16)$$

where  $S_{ij}$  is [25]:

$$S_{ij} = \frac{1}{2} \left( \frac{\partial u_i}{\partial x_j} + \frac{\partial u_j}{\partial x_i} \right) \quad (17)$$

The equation for the heat flux is [25]:

$$q_j = -\kappa \frac{\partial T}{\partial x_j} \quad (18)$$

where  $\kappa$  is the thermal conductivity [25].

The in-house code uses a high-pass filter to separate the scales in these equations [39]. In a general case, the convolution filter that is applied in both time and space is [39]:

$$\bar{\phi}(\vec{x}, t) = \frac{1}{\Delta} \int_{-\infty}^{\infty} \int_{-\infty}^{\infty} G\left(\frac{\vec{x} - \vec{\zeta}}{\Delta}, t - t'\right) \phi(\vec{\zeta}, t') dt' d^3\vec{\zeta} \quad (19)$$

where  $\phi$  is the parameter to be filtered,  $\bar{\phi}$  is its filtered value,  $G$  is the convolution kernel and  $\Delta$  is the filter size [39]. In the code, the filter size is a third of the volume of a cell [39]. The classical filter used is a box filter [39]:

$$G(\vec{x} - \vec{\zeta}) = \begin{cases} \frac{1}{\Delta} & \text{if } |\vec{x} - \vec{\zeta}| \leq \frac{\Delta}{2} \\ 0 & \text{otherwise} \end{cases} \quad (20)$$

This divides each of the flow parameters into the portion of the parameter that is filtered, and the portion that is modeled [39]:

$$\phi = \bar{\phi} + \phi' \quad (21)$$

Since the flow is compressible, a Favre filter is also used to weight the filtered variables by their density [25]:

$$\overline{\rho\phi} = \bar{\rho} + \tilde{\phi} \quad (22)$$

This further decomposes the variables [25]:

$$\phi = \tilde{\phi} + \phi'' \quad (23)$$

where  $\phi$  is the parameter to be filtered,  $\tilde{\phi}$  is the low frequency part and  $\phi''$  is the high frequency part [25]. This leads to the filtered form of the governing equations [39]:

$$\frac{\partial \bar{\rho}}{\partial t} + \frac{\partial \bar{\rho} \tilde{u}_i}{\partial x_i} = 0 \quad (24)$$

$$\frac{\partial \bar{\rho} \tilde{u}_i}{\partial t} + \frac{\partial \bar{\rho} \tilde{u}_i \tilde{u}_j}{\partial x_j} + \frac{\partial \bar{p}}{\partial x_j} - \frac{\partial \check{\sigma}_{ij}}{\partial x_j} = -\frac{\partial \check{\tau}_{ij}}{\partial x_j} + \frac{\partial}{\partial x_j} (\bar{\sigma}_{ij} - \check{\sigma}_{ij}) \quad (25)$$

$$\begin{aligned} \frac{\partial \bar{\rho} \tilde{E}}{\partial t} + \frac{\partial (\bar{\rho} \tilde{E} + \bar{p}) \tilde{u}_j}{\partial x_j} - \frac{\partial \check{\sigma}_{ij} \tilde{u}_i}{\partial x_j} + \frac{\partial \check{q}_j}{\partial x_j} = \\ - \frac{\partial}{\partial x_j} \left[ \left( \overline{\rho u_j E} - \bar{\rho} \tilde{u}_j \tilde{E} \right) + (\overline{u_j p} - \tilde{u}_j \bar{p}) - (\overline{\sigma_{ij} u_j} - \check{\sigma}_{ij} \tilde{u}_j) - (\bar{q}_j - \check{q}_j) \right] \end{aligned} \quad (26)$$

where

$$\check{\sigma}_{ij} = \mu \left( \tilde{T} \right) \left( 2\tilde{S}_{ij} - \frac{2}{3} \delta_{ij} \tilde{S}_{kk} \right) \quad (27)$$

and

$$\check{q}_j = -\kappa \left( \tilde{T} \right) \frac{\partial \tilde{T}}{\partial x_j} \quad (28)$$

The sub-grid scale terms can then be gathered into one equation [25]:

$$\left( \overline{\rho u_j E} - \bar{\rho} \tilde{u}_j \tilde{E} \right) + (\overline{u_j p} - \tilde{u}_j \bar{p}) = C_p Q_j + \mathcal{J}_j \quad (29)$$

where  $C_p$  is the specific heat at constant pressure,  $Q_j$  is the sub-grid scale temperature flux defined as [25]:

$$Q_j = \bar{\rho} \left( \widetilde{u_j T} - \tilde{u}_j \tilde{T} \right) \quad (30)$$

and  $\mathcal{J}_j$  is the turbulent diffusion defined by [39]:

$$\mathcal{J}_j = \frac{1}{2} (\bar{\rho} u_j \widetilde{u_i u_i} - \bar{\rho} \tilde{u}_j \tilde{u}_i \tilde{u}_i - \tau_{ii}) \quad (31)$$

The sub-grid scale viscous diffusion is included as the third term on the right-hand side of the filtered energy equation, Equation 26 [39]:

$$\mathcal{D}_j = \overline{\sigma_{ij} u_j} - \check{\sigma}_{ij} \tilde{u}_j \quad (32)$$

These two equations for sub-grid scale diffusion can be added back into the equation for total energy [39]:

$$\begin{aligned} \frac{\partial \bar{\rho} \tilde{E}}{\partial t} + \frac{\partial (\bar{\rho} \tilde{E} + \bar{p}) \tilde{u}_j}{\partial x_j} - \frac{\partial \check{\sigma}_{ij} \tilde{u}_i}{\partial x_j} + \frac{\partial \check{q}_j}{\partial x_j} = \\ - \frac{\partial}{\partial x_j} [C_p Q_j + \mathcal{J}_j - \mathcal{D}_j - (\bar{q}_j - \check{q}_j)] \quad (33) \end{aligned}$$

### 3.2.1 Subgrid Scale Models

To use the sub-grid scale models, the momentum equation has to be further simplified [39]. It can be noted that the second term on the right-hand side of the filtered momentum equation is negligible compared to the first [39]. The stress tensor can thus be rewritten as [39]:

$$\tau_{ij} = \mu_{SGS} \left( \frac{\partial \tilde{u}_i}{\partial x_j} + \frac{\partial \tilde{u}_j}{\partial x_i} \right) - \frac{2}{3} \mu_{SGS} \operatorname{div} \tilde{\mathbf{u}} \quad (34)$$

The wall-adapting local eddy viscosity (WALE) model is used to predict the behavior of the eddy viscosity near the wall [39]. WALE was suggested by Nicoud et al. as a model based on vorticity and strain rate [50]. In the WALE model, the eddy viscosity is based on the square of the velocity gradient tensor [50]. This provides the equation for the viscosity term [39]:

$$\mu_{SGS} = \rho (C_w \Delta)^2 \frac{(S_{ij}^d S_{ij}^d)^{\frac{3}{2}}}{\left(\tilde{S}_{ij} \tilde{S}_{ij}\right)^{\frac{5}{2}} + (S_{ij}^d S_{ij}^d)^{\frac{5}{4}}} \quad (35)$$

where

$$C_w \sim \sqrt{10.6} C_S \quad (36)$$

$$S_{ij}^d = \tilde{S}_{ik} \tilde{S}_{kj} + \tilde{\Omega}_{ik} \tilde{\Omega}_{ik} - \frac{1}{3} \delta_{ij} \left[ \tilde{S}_{mn} \tilde{S}_{mn} - \tilde{\Omega}_{mn} \tilde{\Omega}_{mn} \right] \quad (37)$$

$$\tilde{\Omega}_{ij} = \frac{1}{2} \left( \frac{\partial \tilde{u}_i}{\partial x_j} - \frac{\partial \tilde{u}_j}{\partial x_i} \right) \quad (38)$$

where  $C_S$  is the Smagorinsky constant (equal to 0.15 in the in-house code) and  $\tilde{\Omega}_{mn}$  is vorticity correspond to filtered velocity [39].

### 3.3 Discretization

The in-house code is used to solve the governing equations. The in-house code uses both finite element and finite volume discretization.

Non-linear terms need to be discretized using the more robust finite volume [39]. The convection and temporal terms are therefore discretized using a finite volume approach [39]. Finite element discretization is more straightforward and can be used for linear calculations. Finite element methods are used to model the remaining terms

- diffusion, the viscous fluxes, and the source term [39]. This division of discretization types is a conventional approach, used in commercial software [6].

The discretization low-dissipative, upwind, and second order in both time and space [39]. In time, second order is the minimum order possible to obtain accurate results from LES [39]. The order is second in space to encourage the accuracy of the results, while the upwind method was chosen over a central differencing method to maintain the simulations stability and convergence.

A tetrahedral and unstructured mesh are both requirements of the in-house code. The mesh needs to be unstructured because this way ICEM will store information about the connectivity between the grid elements, while tetrahedral cells are assumed in the discretization of the governing equations. The governing equations are solved for each of the cells, and the code calculates the viscous fluxes in and out of each cell. The computing can then be done in parallel, using MPI. Partitioning was done using Metis 4.0. For each partition, the code user receives information about the mesh node coordinates, the distance from each node to the closest wall, and information about how the mesh in the partition relates to the other partitions, especially with respect to periodic boundaries.

### 3.4 Time Step Size

The time step required for this simulation is calculated by the in-house code and is not selected by the user. It is based on the Courant (CFL) number. For implicit schemes, the time step is limited by:

$$CFL = \frac{u\Delta t}{\Delta x} \quad (39)$$

Limiting the time step this way ensure that the time step size is less than the time required to transfer information from one cell to the next, and is thus limited

by the mesh [39]. The code looks through each of the cells and finds the time needed to diffuse and convect information to the neighbouring cells. The smallest time value found is used as the time step size for the entire grid.

## **3.5 Meshing Considerations**

### **3.5.1 Domain Size**

To accurately capture all the aerodynamic processes, the domain was created to be 20 times the chord in the radius. 20 times the chord was chosen to be the domain length so that it would be large enough that the boundary conditions do not have a direct effect on the flow around the airfoil: the flow around the airfoil is not forced to conform to the boundary conditions, and the flow can fully develop.

### **3.5.2 Cell Size at the Wall**

The  $y+$  value is maintained at or below one in the first cell off the wall, and the aspect ratio is kept below 20 per LES requirements.

## **3.6 Boundary Conditions**

### **3.6.1 Periodic Condition**

The periodic boundary condition is applied to the faces in the span direction. The domain is in 2.5D, to reduce computational costs. This means that the fluxes that exit out of one periodic face are equal to the fluxes that enter on the other side.

### **3.6.2 Walls**

There is a no-slip condition on the surface of the airfoil. This is because, for a viscous fluid, fluid molecules stick to the surface past which they are flowing, and thus have no velocity there. This leads to a boundary layer at the wall. The walls are also set to adiabatic for these simulations.

### **3.6.3 Far-Field Condition**

The outlet and the remaining faces are deemed a far field boundary condition, with the pressure there being equal to atmospheric.

### **3.6.4 Inflow**

The air flowing into the domain was given a Reynolds number and a Mach number, which provided the code with an incoming velocity. No incoming turbulence was implemented for these simulations as it is not yet available in the in-house code.

## **3.7 Mesh Deformation**

The coordinates of the deforming airfoil in each of its deformed positions are inputted into the code. A Fourier equation for the curve of the airfoil is found based on these points and can be seen in more detail in the Appendix. A specific boundary condition is applied to the mesh where the deformation is to take place. Each iteration, the code moves the points of the airfoil toward its next frame. The mesh allows this to happen using smoothing. The two types of smoothing implemented in the in-house code are diffusion smoothing and spring-based smoothing.

### 3.7.1 Diffusion Smoothing

Diffusion smoothing involves solving the Laplace equation:

$$\begin{cases} \Delta \cdot (\gamma \Delta u) = 0 & \Omega \\ u = f & \delta\Omega \end{cases} \quad (40)$$

where  $\Omega$  is the computational domain, and  $\gamma$  is defined as:

$$\gamma = \frac{1}{d^n} \quad (41)$$

where  $d$  is the distance between two points.

The amount of deformation that takes place for each tetrahedron depends on its distance to a prescribed point or boundary. Both the surface of the airfoil and the tip of the airfoil were used to measure the distance - however, for this case, this resulted in negative volumes being created in the mesh. Diffusion smoothing is therefore not used for mesh deformation in this study.

### 3.7.2 Spring-Based Smoothing

When a node in the mesh moves, a force is created on that node [6]. The larger the displacement, the larger the force [6]. Based on Hooke's Law, the equation for the force on a mesh node is [6]:

$$\vec{F}_i = \sum_j^{n_i} k_{ij} (\Delta \vec{x}_j - \Delta \vec{x}_i) \quad (42)$$

$$k_{ij} = \frac{1}{d_{ij}} \quad (43)$$

where  $k$  represents the spring stiffness [39].

It was found that when a mesh of sufficient quality was created - particularly if the cells near the trailing edge were almost perfectly square - the spring-based smoothing

method would allow the mesh to deform. Therefore the spring-based smoothing method is used for this project.

### 3.8 Force Calculations

In order to obtain quantitative results from CFD simulations, forces have to be extracted from the flow field. Force components are calculated along a vector direction, and are the sum of the dot product of pressure and viscous forces [6]:

$$F_a = \vec{a} \cdot \vec{F}_p + \vec{a} \cdot \vec{F}_v \quad (44)$$

where  $F_a$  is the total force along  $\vec{a}$ ,  $F_p$  is the pressure force, and  $F_v$  is the viscous force. The pressure and the viscosity are calculated separately. The pressure is calculated based on Equation 12. The viscosity is calculated using the Reynolds number inputted by the user. The equation for the Reynolds number is:

$$Re = \frac{\rho ul}{\mu} \quad (45)$$

where  $l$  is the characteristic length, and  $\mu$  is the required viscosity.

Once the forces are obtained, the coefficients can be calculated by dividing the force by  $\frac{1}{2}\rho v^2$ . The force coefficients in the lift and drag directions are computed at each iteration by the in-house code.

# Chapter 4

## LES Validation

Due to the nature of CFD simulations, models need to be validated for accuracy before they can be used. In this chapter, the ability of the code to capture laminar to turbulent transition and to provide results similar to experiment is verified.

### 4.1 Experimental Comparison

#### 4.1.1 Experimental Setup

In 2011, Li et al. published a paper titled “Effect of turbulence intensity on airfoil flow: numerical simulations and experimental measurement” [44]. Li et al.’s experiments measured the lift and drag coefficients of a NACA0012 airfoil at different angles of attack at a Reynolds number of 5,300 [44]. The mean stream-wise velocity was captured using 450 images, as the turbulence intensity was varied between 0.6% and 6% [44]. The resulting lift curve slopes can be seen in Figure 16.

#### 4.1.2 WALE Simulation

A simulation using the in-house code was run by the research group maintaining similarity with Li et al.’s experiment. The mesh is an o-grid with 14,112,322 elements

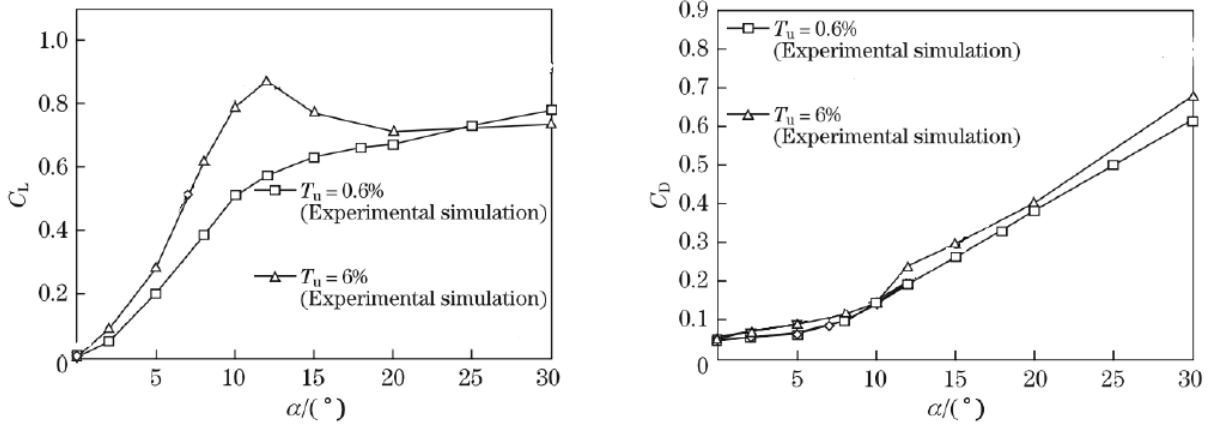


Figure 16: Lift and drag curve slopes of a NACA0012 airfoil at a Reynolds number of 5,300, modified for readability from [44]

and 2,406,080 nodes.

Figure 17 compares the results obtained by the simulation with the experimental results obtained by Li et al. for a flow with 0.6% turbulence intensity [44]. In Figure 17 it can be seen that the experimental results are very similar to the LES results until the angle of attack passes  $10^\circ$ .

This difference is likely due to the difference in turbulence intensity between the simulations and the experiments. Figure 16 shows how sensitive the aerodynamics of the airfoil is to the energy of the flow.

## 4.2 Laminar to Turbulent Transition

The in-house code can also capture the transition from laminar to turbulent flow. A static simulation was performed with a NACA0012 airfoil at a  $10^\circ$  angle of attack.  $10^\circ$  is past the critical angle for a NACA0012, and thus can be used to see whether the in-house code can visualize transition.

The simulations were set up according to the requirements in Chapter 3. The mesh has 443,900 nodes and 2,567,534 elements. Four points along the airfoil chord were chosen to demonstrate the ability of the in-house code to visualize laminar to

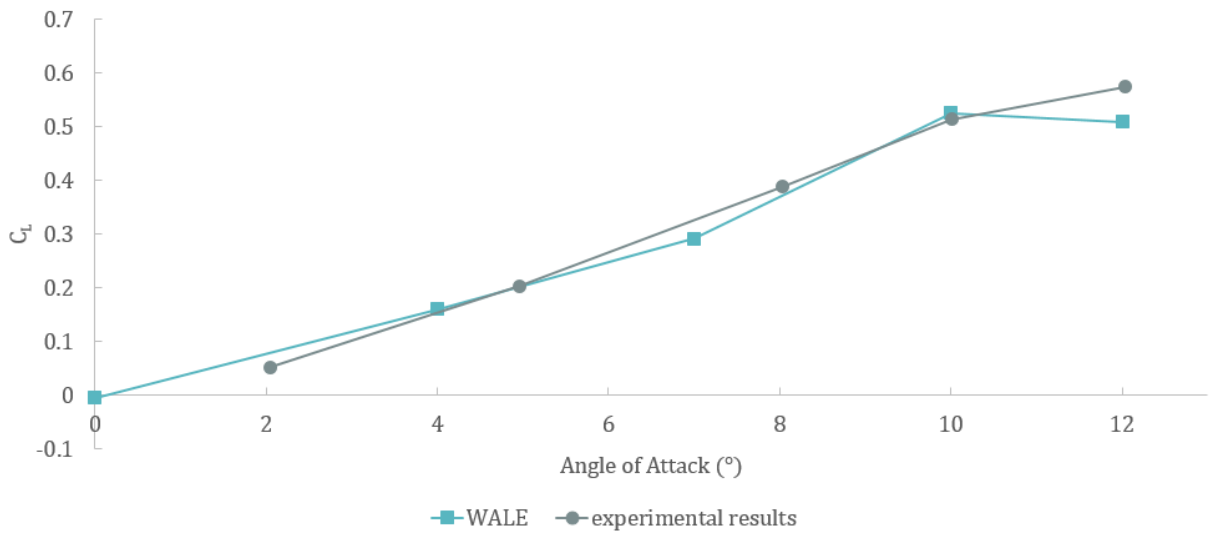


Figure 17: comparing experimental results with WALE simulations

turbulent transition. These points can be seen in Figure 18. The results of this study can be seen in Figure 19.

It can be seen in Figure 19 that, the further down the airfoil chord a point is located, the more the velocity there varies with time. At P1, the flow is relatively steady, and the velocity does not differ much. This point is located outside of the boundary layer. At P2, transition begins but is not very strong. At P3 and P4, transition is occurring with the velocity varying in a sinusoidal shape.

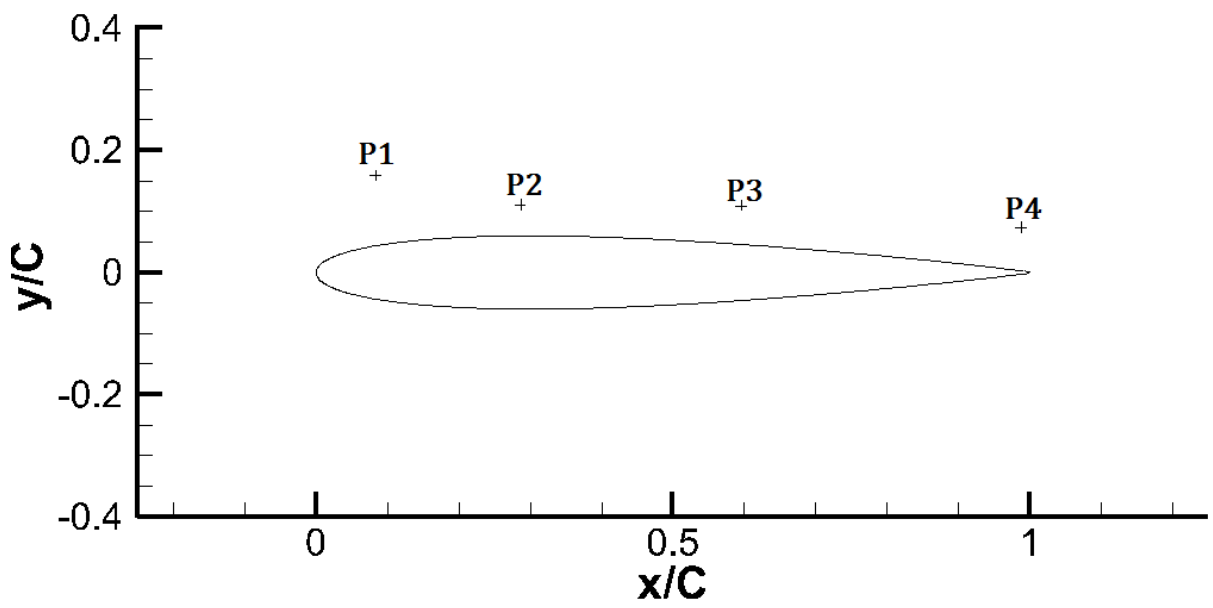


Figure 18: the locations of where the velocity is being measured in time for the laminar to turbulent transition investigation

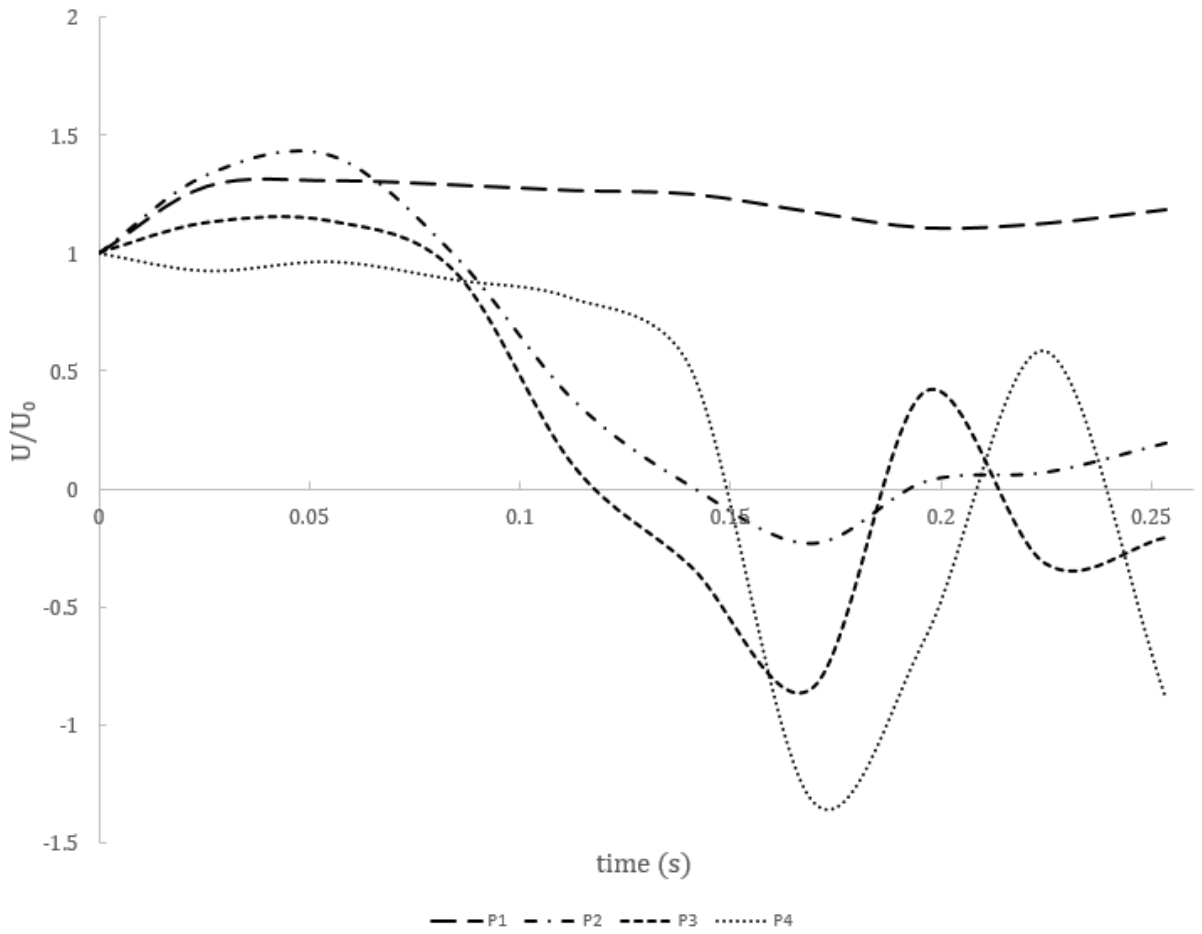


Figure 19: changes in velocity with time during laminar to turbulent transition

# Chapter 5

## Oscillating Case

In “An insight into the dynamic stall lift characteristics”, Choudhry et al. performed a water channel experiment at the University of Adelaide to visualize the vortices present in the dynamic stall process [14]. Those experimental results will be used as a benchmark and compared to the results of LES.

### 5.1 Experimental Setup and Results

Choudhry et al.’s experiment was a hydrogen bubble flow visualization in a  $0.25\text{ m}^2$  working section of a closed-return channel, of a NACA0012 airfoil pitching  $50^\circ$  [14]. The airfoil was pitched with a reduced frequency of 0.1, and a Reynolds number of 10,000 [14]. The flow had an incoming turbulence intensity of 0.6% [14].

The results of these experiments can be seen in Figure 20. Each image represents an increase in angle of attack of  $5^\circ$ . The items of interest are how the vortices appear, grow, and move down the airfoil as it pitches. These are all aspects that are important for a CFD code to detect, and therefore to prove that the in-house code is accurate enough to predict dynamic stall.

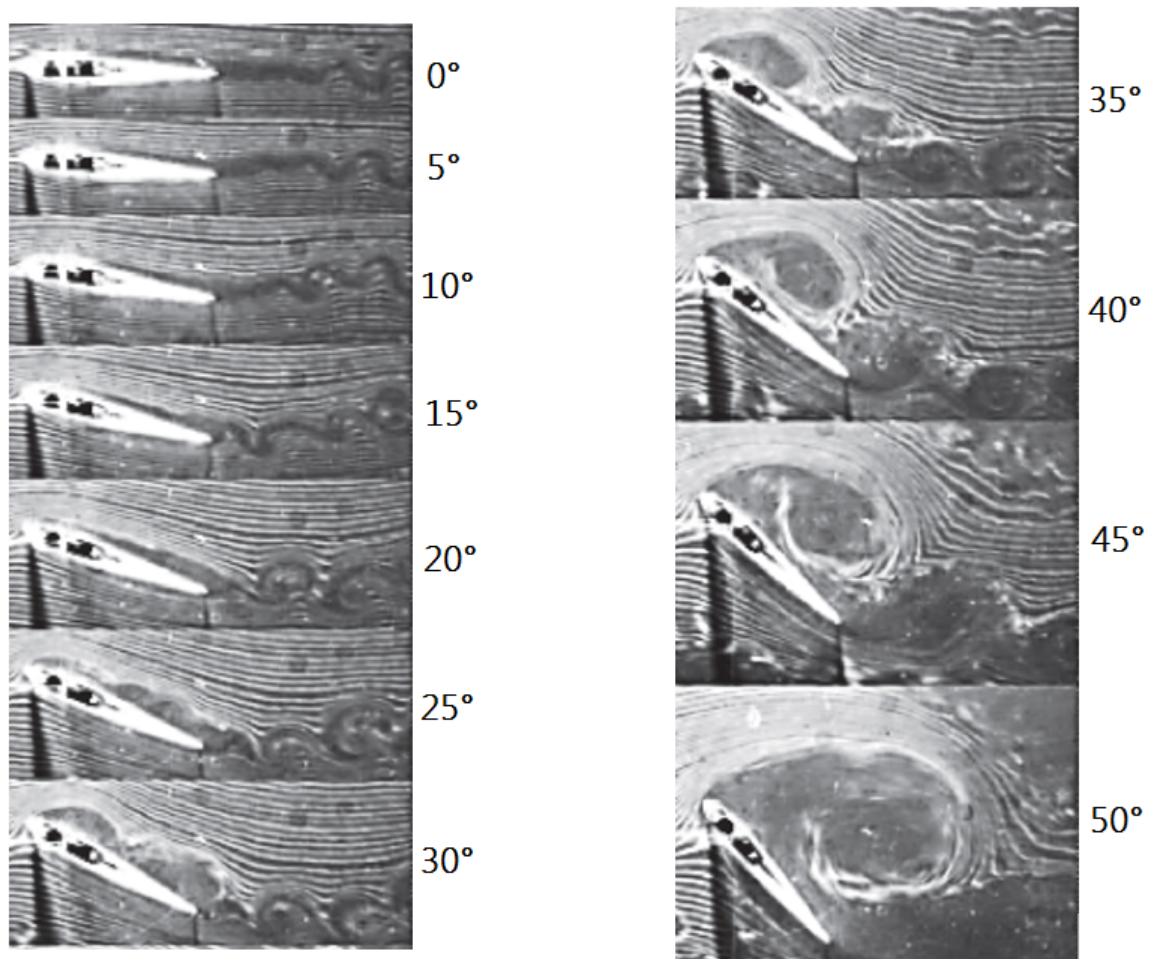


Figure 20: experimental results obtained using PIV by Choudhry et al. Starting at 0°, each image is associated with a 5° increase in angle of attack [14]



Figure 21: a NACA0012 airfoil

## 5.2 Geometry

The coordinates for a NACA0012 airfoil were obtained from the Cambridge-MIT Institute [34]. This geometry has a sharp trailing edge, which was chosen to simplify the creation of the mesh. The airfoil coordinates were non-dimensionalized, so its length is a unit of one. An image of the airfoil can be seen in Figure 21.

## 5.3 Computational Domain

As described in Chapter 3, the computational domain is 20 times the chord length. The length of the spanwise direction is 20% of the chord length. An image of the domain can be seen in Figure 22.

## 5.4 Mesh

To perform this validation, a mesh was created using ANSYS ICEM. The periodic, discretization, and cell size conditions described in Chapter 3 were all used in its construction. Since LES was used, the aspect ratio of the cells off the airfoil was calculated. The largest aspect ratio of any cell was 16.5. Images of the mesh can be seen in Figures 23 a), b), and c).

Figure 23 a) shows a large overall image of the meshed domain. Figure 23 b) shows a closeup view of the boundary layer at the tail, the sharp trailing edge, and how the mesh looks in the spanwise direction. Figure 23 c) shows the mesh around

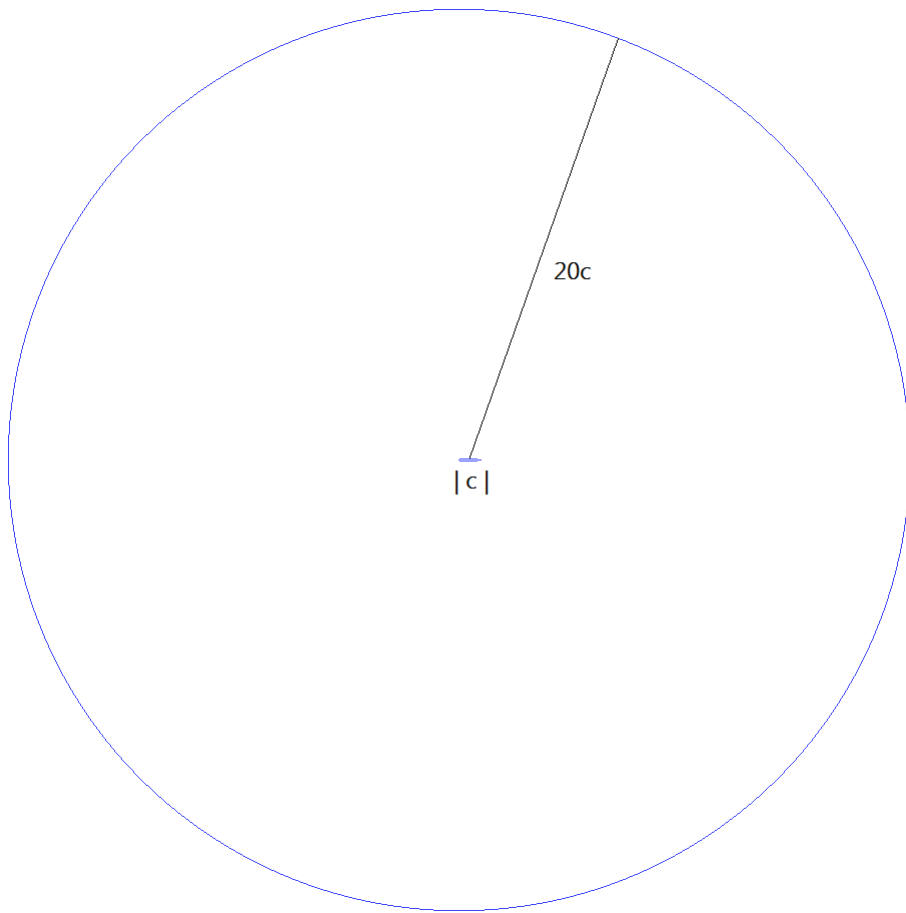


Figure 22: the computational domain with the airfoil at the center

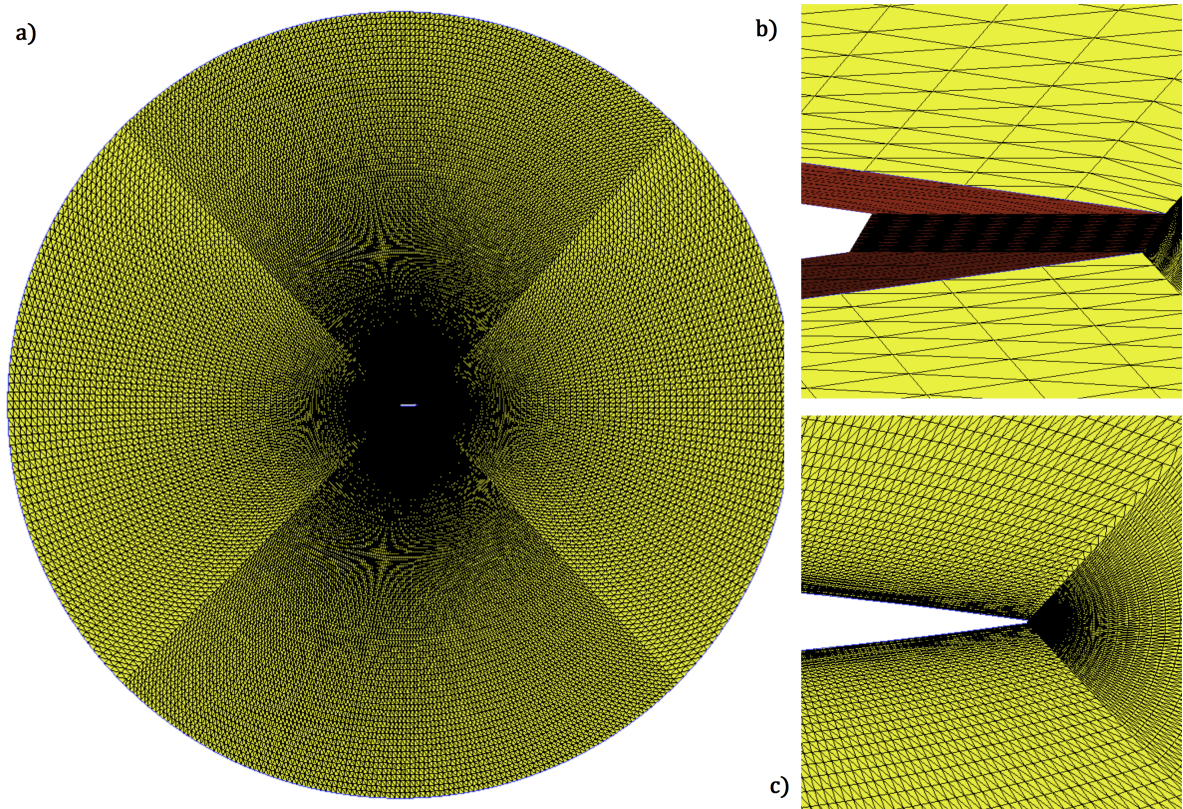


Figure 23: overall and close-up view of the computational mesh

the trailing edge, and how the size of the cells grow as you get further from the airfoil surface.

The mesh has 443,900 nodes and 2,567,534 elements. The maximum aspect ratio size limited the cell size off the airfoil, and by requiring the  $y+$  value to be below one. After the first limited cell size, each cell after that grows by 10%. This ensured that the cells were small enough to capture the flow, but the mesh away from the airfoil would not be too fine.

Due to the discretization methods in the in-house code, the cells are unstructured tetrahedrons.

## 5.5 Setup

A comparison can be made by using non-dimensional number similarity. Reynolds number and reduced frequency similarity are maintained. The boundary conditions described in Chapter 3 were used.

The Mach number is used to calculate the incoming flow speed. These simulations have a freestream Mach number of 0.1; effects on the dynamic stall vortex have not been noted at Mach numbers of this size [13].

Up to 200 inner loop iterations are completed for each cycle. The convergence criteria for an inner loop cycle was  $1.0 \times 10^{-6}$ . The CFL number for this simulation was started at 1 and was allowed to increase at each iteration up to a value of 125. This was found to be the highest CFL number that could be used without the results diverging.

## 5.6 Oscillation Calculation

The oscillation is performed using the whole domain. At each iteration, the domain and the mesh are rotated a fraction of the desired amplitude, based on the completed fraction of time in the period. The fraction of time passed provides the code with an angle for the domain. With this angle, a velocity is calculated at each node to move the mesh. This method is preferable to moving the airfoil, as it does not require the mesh to deform, and is simpler than changing the boundary conditions with time.

## 5.7 Computational Time

To match the experiments performed by Choudhry et al., the simulations were set up to oscillate to a  $50^\circ$  angle of attack, with a period of 1.84 seconds. Initially, the Euler equations were used to perform the simulations, because the Euler equations

can be solved much faster, and the beginning of a simulation is often unphysical, and the initial results would therefore not be used. Two cycles were completed using the Euler equations. The in-house code does not calculate any forces while using these equations, because when Euler equations are used the viscous forces cannot be calculated. Once the airfoil returned to the initial angle of attack for the third time, the viscosity terms were turned on.

Each Euler cycle took approximately three weeks to complete, while one viscous cycle took six weeks on Compute Canada’s Cedar high-performance computer, using 144 processors. This is computationally very expensive and limited the number of cycles that could be simulated.

## 5.8 Convergence

Generalized Minimum Residual Algorithm (GMRES) is used to determine convergence [39]. The linear residual criteria inside GMRES is  $1.0 \times 10^{-6}$ .

## 5.9 Results

First, the features of the flow will be analyzed. Figure 24 shows the pressure contours around the oscillating NACA0012 at  $0^\circ$ ,  $10^\circ$ ,  $15^\circ$ ,  $20^\circ$ ,  $30^\circ$ ,  $40^\circ$ , and  $50^\circ$  angle of attack. There is good agreement between these simulation results and the PIV images shown by Choudhry et al., but there is a small difference in the behaviour of the vortex. At  $20^\circ$ , the flow has separated, and there is a separation bubble visible at the leading edge of the airfoil, as well as a second vortex further down. At a  $30^\circ$  angle of attack, both the leading edge separation bubble and the vortex partly down the airfoil have grown, with the vortex slightly larger than the separation bubble. In both the PIV and the LES simulations, there are the two vortices over the airfoil as well as another coming from the trailing edge. At  $40^\circ$ , there is one large circulating vortex coming

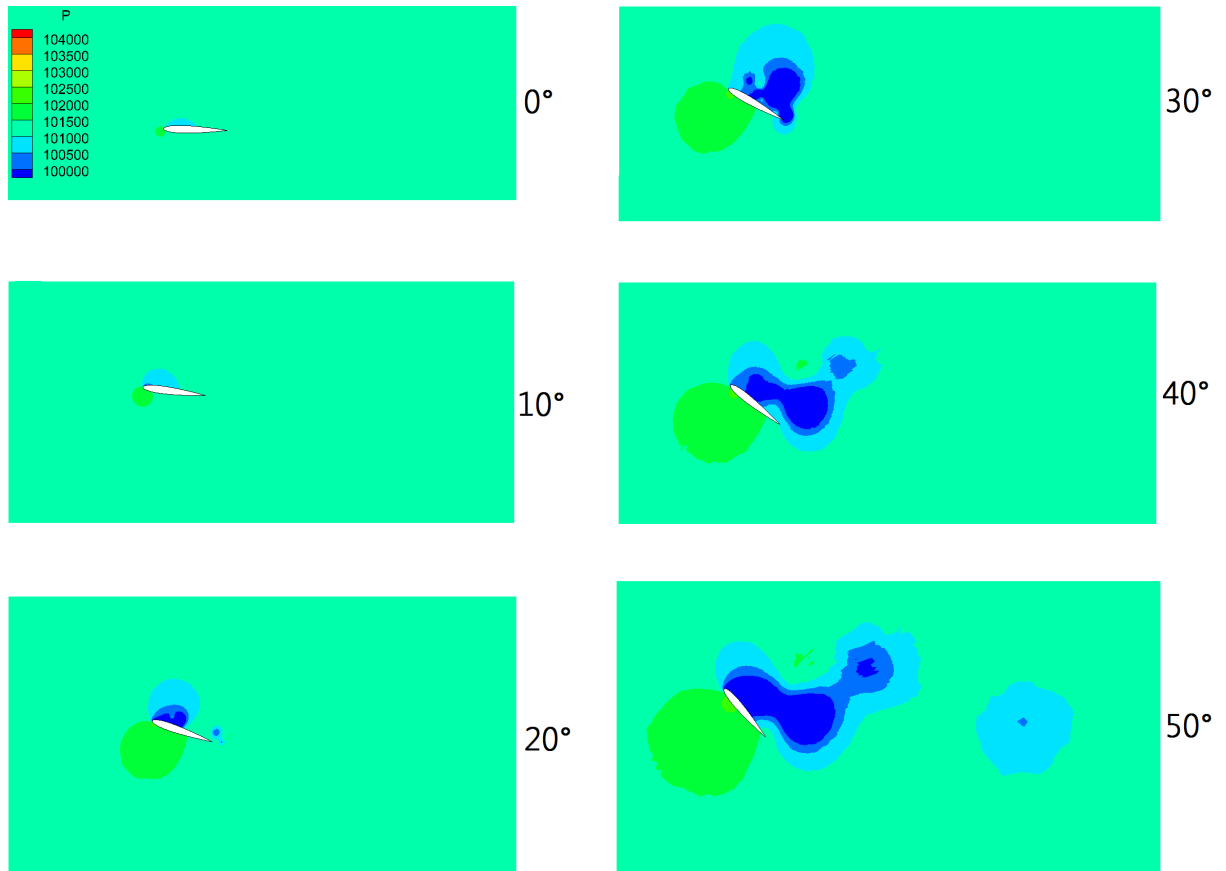


Figure 24: pressure contours showing the vortex growth visualized by the in-house LES code

from the leading edge of the airfoil, as well as some circulation at the leading edge. And, at a  $50^\circ$  angle of attack, the separation bubble and the vortex have completely merged into the largest vortex seen.

However, there are a few noticeable differences between the PIV images and the LES results. At the  $20^\circ$  angle of attack, in the PIV images, this second vortex appears at approximately  $0.4c$ , while the LES simulations have it appearing much closer to the leading edge. Also, the vortices that move upward, away from the airfoil in the LES simulations cannot be seen in the PIV images.

The streamlines provide an even better picture of what is happening in the flow. As demonstrated in Figure 26, at  $30^\circ$ , it is encouraging to see that the LES has succeeded in capturing two vortices attached to the airfoil, but the LES includes a

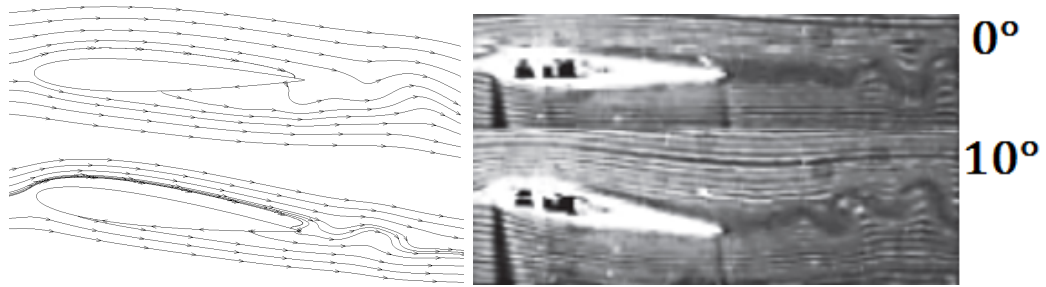


Figure 25: comparing the streamlines and the PIV images at  $0^\circ$  and  $10^\circ$  angle of attack

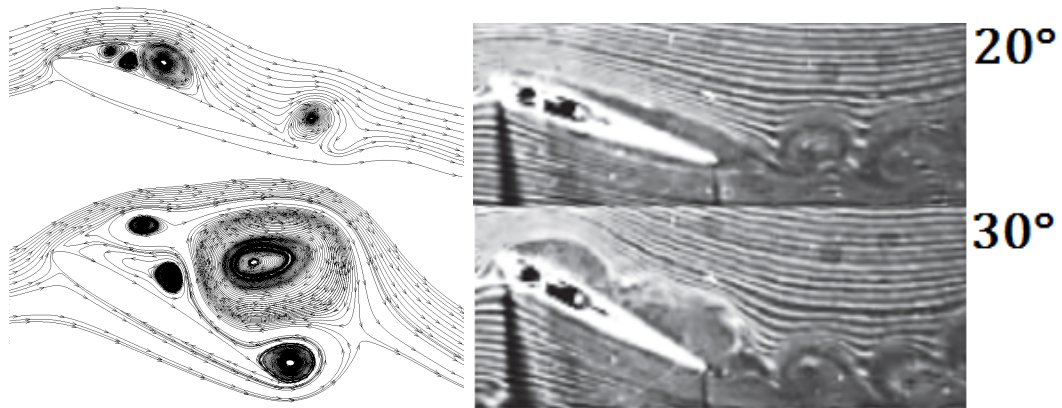


Figure 26: comparing the streamlines and the PIV images at  $20^\circ$  and  $30^\circ$  angle of attack

third vortex in the center that is not seen by the PIV images. The vortex that was in the location at  $30^\circ$  then detaches from the airfoil to become its own vortex, as can be seen in Figure 27. This vortex remains touching the airfoil in the PIV images. At 50 degrees angle of attack, there is just one vortex as expected, but the flow in the LES simulation remains attached at the trailing edge, while in the PIV images it is detached. This can be seen in Figure 27.

The LES results and the PIV images have the same main features, but those features appear at a lower angle of attack in the LES simulations. This is likely because flows are very sensitive to the incoming turbulence intensity [44]. The LES simulations do not have any incoming turbulence, whereas the water tunnel experiments have an incoming turbulence intensity of 0.6%. This explains why vortices simulated

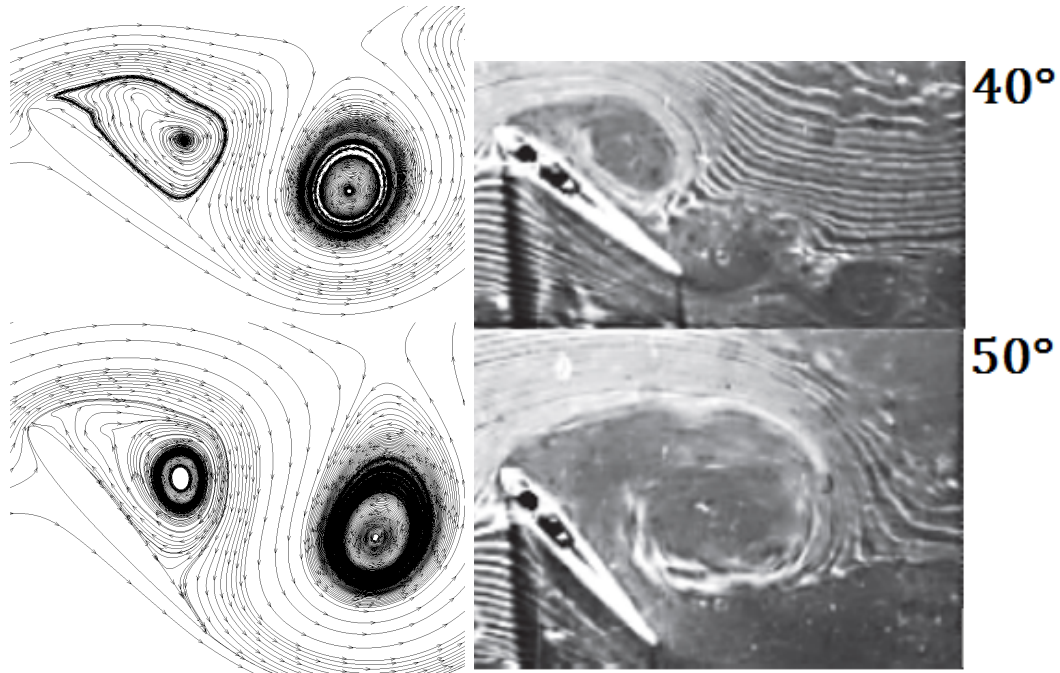


Figure 27: comparing the streamlines and the PIV images at  $40^\circ$  and  $50^\circ$  angle of attack

by LES detach, while in the water tunnel do not: the boundary layer was not forced downward by turbulence [44]. Additionally, in the simulations the airfoil is rotated from the leading edge, whereas the experimental airfoil was rotated from the quarter chord point. These would have provided the same results had the experiments been static, but since they are dynamic, the simulated airfoil has to travel further than the experimental one. This affects the vortex generation.

Despite these discrepancies, the LES do well at simulating the leading edge of the airfoil. This is significant because the majority of the lift of an airfoil when it is pitching comes from the leading edge, and not from where the flow has separated.

### 5.9.1 Aerodynamic Forces based on Angle of Attack

Figure 28 shows how the coefficients of lift and drag vary with angle of attack, based on the simulations performed. For static NACA0012 airfoils, stall happens at less than  $10^\circ$  for a Reynolds number of 50,000. For this oscillating case, stall does not occur

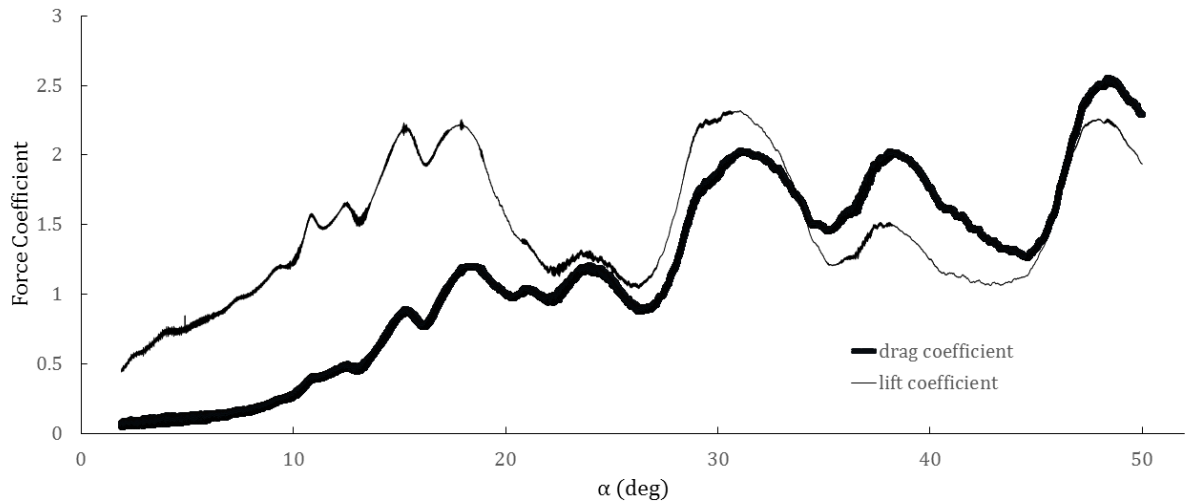


Figure 28: the lift and drag coefficients with angle of attack for the oscillating airfoil until approximately  $17^\circ$ , and even then it recovers back to its previous lift coefficient at  $27^\circ$  degrees. This graph is similar to the sample graph shown by Choudhry et al. as an example of the lift curve slope of an airfoil undergoing dynamic stall, as can be seen in Figure 29 [14]. That figure shows averages of the  $C_L - \alpha$ , based on multiple experiments.

These aerodynamic forces correspond to the changes in the coefficient of pressure that can be seen in Figure 30. As can be seen in that Figure, the higher the angle of attack of the airfoil, the greater the variation of the pressure coefficient.

At  $0^\circ$  and  $10^\circ$ , there is no vortex formation, so the pressure coefficient with chord is a relatively straight line, with little variation except for at the leading and trailing edges.

At  $20^\circ$ , the vortex formation has occurred at the first half of the airfoil, leading to much lower pressure for the first half of the chord, but dropping after that since the flow at the latter half of the chord is still attached. At the trailing edge, there is another vortex, and then pressure there drops as well.

At  $30^\circ$ , the first vortex seen in the streamlines has left the leading edge - there are only two vortices left, one at the mid-chord location and one at the trailing edge.

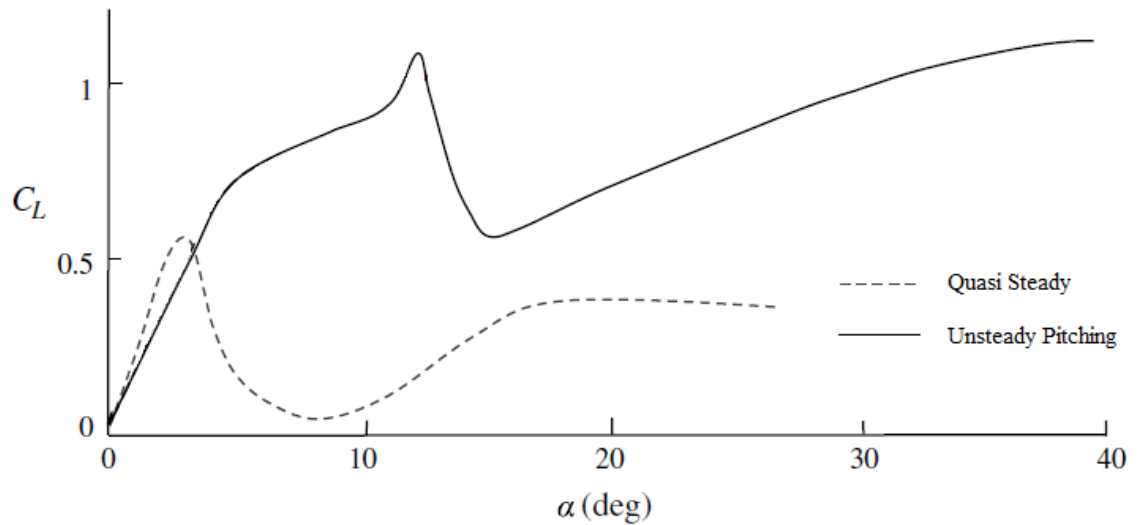


Figure 29: comparing the  $C_L - \alpha$  curve for an airfoil when it is quasi steady, versus when it is pitching unsteadily [14]

This explains why the pressure at the leading edge of the airfoil is not as low at  $30^\circ$  as it was at  $20^\circ$ . The vortex at the trailing edge is larger, leading to the highest pressure seen there so far.

The vortex at the leading edge of the airfoil at  $40^\circ$  is larger and closer than it was at  $30^\circ$ , leading to lower pressure shown in the  $C_p$  graphs.

Finally, at  $50^\circ$ , there is a big vortex that keeps the pressure very low. It is over most of the airfoil, though the flow reattaches at the tail. The pressure over this airfoil is the lowest due to the large vortex, and this can be seen in the  $C_p$  graphs.

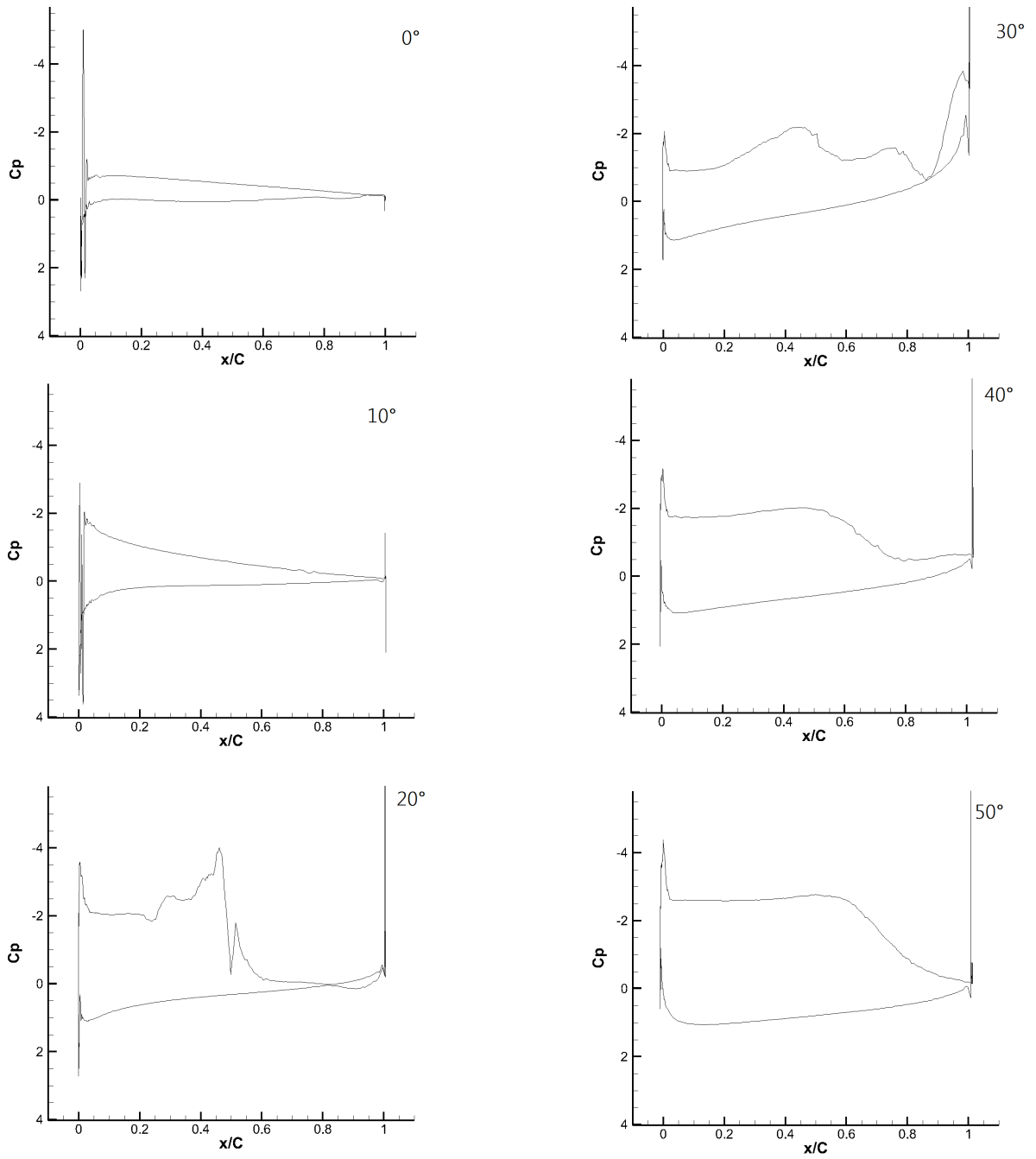


Figure 30: the  $C_p$  curves for the oscillating airfoil

# Chapter 6

## Deforming Case

Now that the LES models have been verified, simulations and analysis of the deforming airfoil can be completed.

### 6.1 Geometry

The rigid, deforming airfoil from the University of Michigan is similar to the NACA0012 in its undeformed state. However, it also contains 20 other frames that represent the various levels of deformation [51]. These frames can be seen in the Appendix. The extremes of the airfoil deformation can be seen in Figures 31 and 32. The airfoil deforms  $2.7^\circ$  upward and  $5.8^\circ$  degrees downward.

### 6.2 Computational Domain

As described in Chapter 3, the computational domain is 20 times the chord length. An image of the domain can be seen in Figure 22.

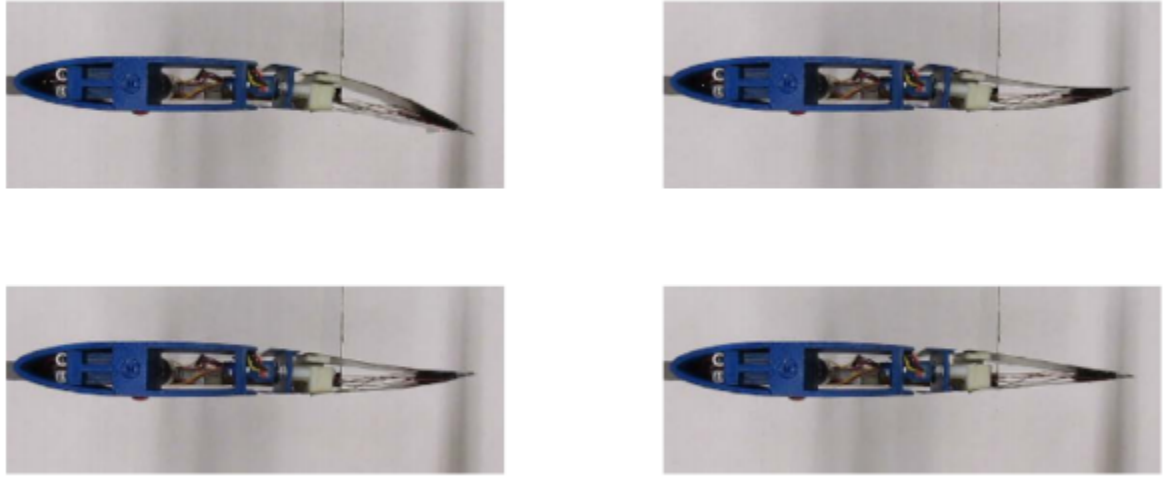


Figure 31: the SSMA created by Pankonien et al. [51]

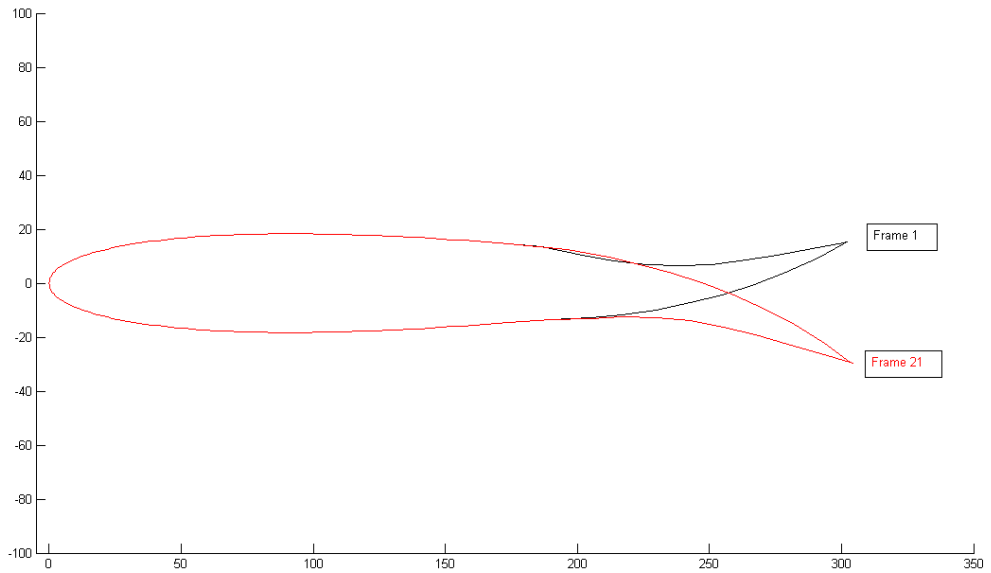


Figure 32: the extremes of the deforming airfoil

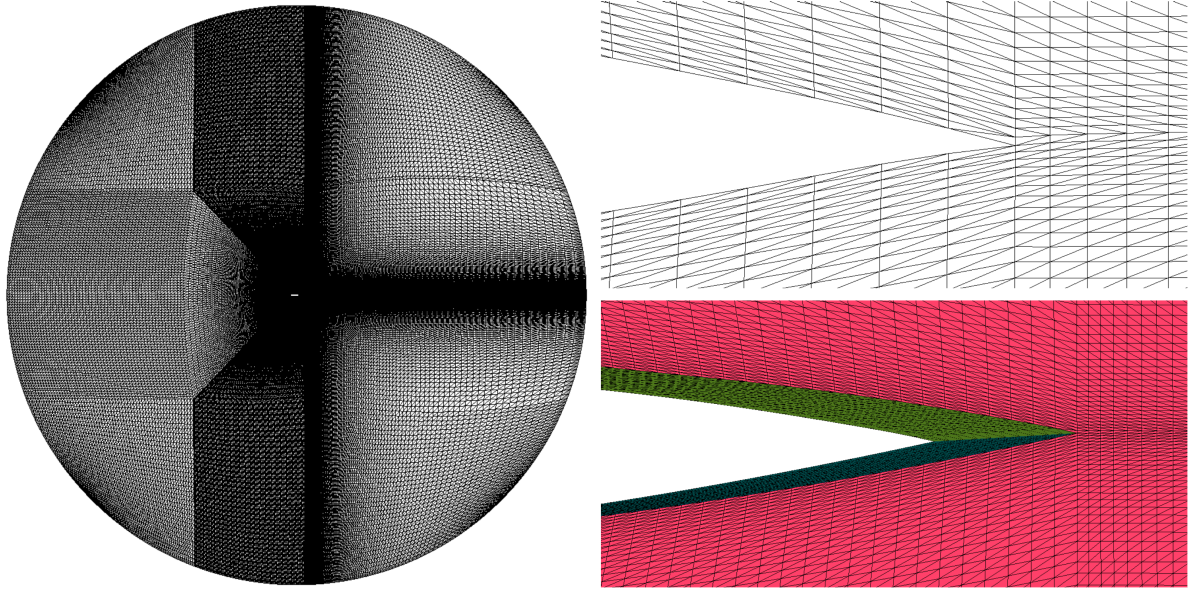


Figure 33: overall and close up views of the mesh for the deforming airfoil

### 6.3 Mesh

The mesh was created using ANSYS ICEM. It contains 5,288,364 elements and 911,141 nodes. The shape of the cells is tetrahedral, and the mesh is unstructured.

The aspect ratio of the cells off the airfoil is a maximum of 16.5. The tallest and thinnest cells are the furthest from the airfoil, where the cell aspect ratio is the least important in the static airfoil case. Along the surface of the airfoil, the cells are sized to maintain the  $y+$  value. There is a layer of cells of this size that is three cells in height, after which the cells begin to grow.

It was discovered that for the spring method to work, the mesh at the tip of the airfoil needs to be as square as possible. If the mesh at the tip is not square, when the airfoil deforms, the mesh near the airfoil moves faster than it does further away, creating an area of negative volume.

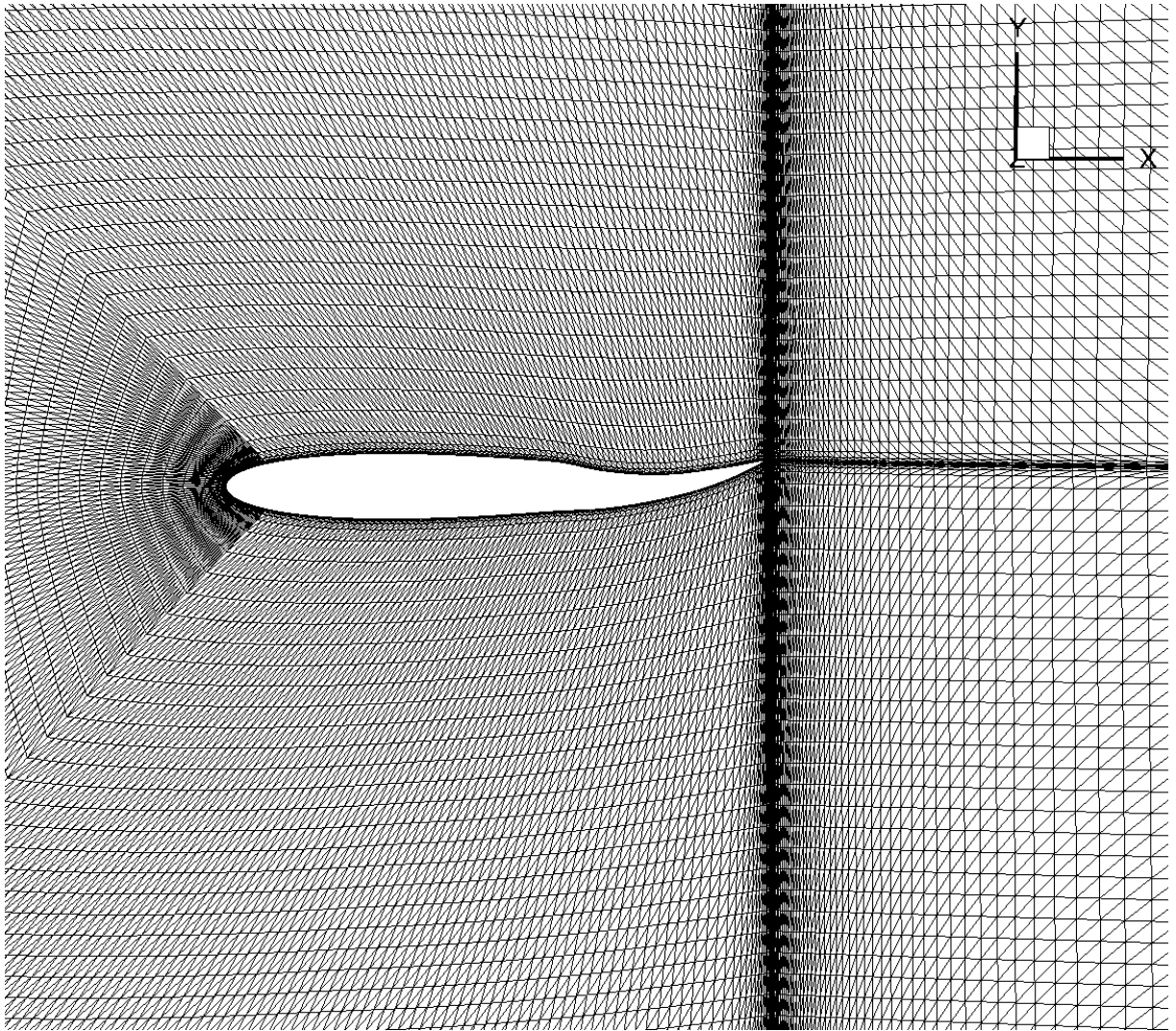


Figure 34: the mesh around the airfoil when it has morphed completely upward

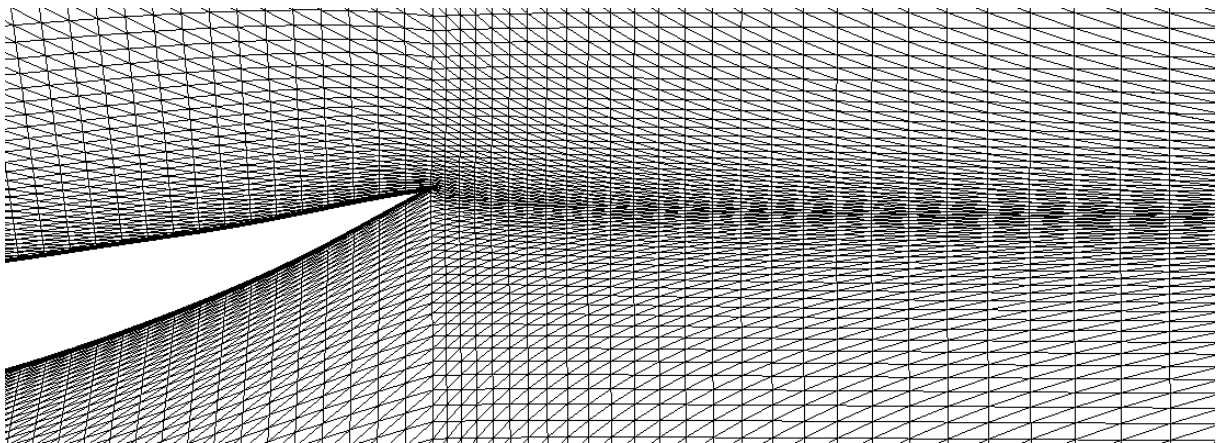


Figure 35: the mesh around the tail when the airfoil is deformed completely upward

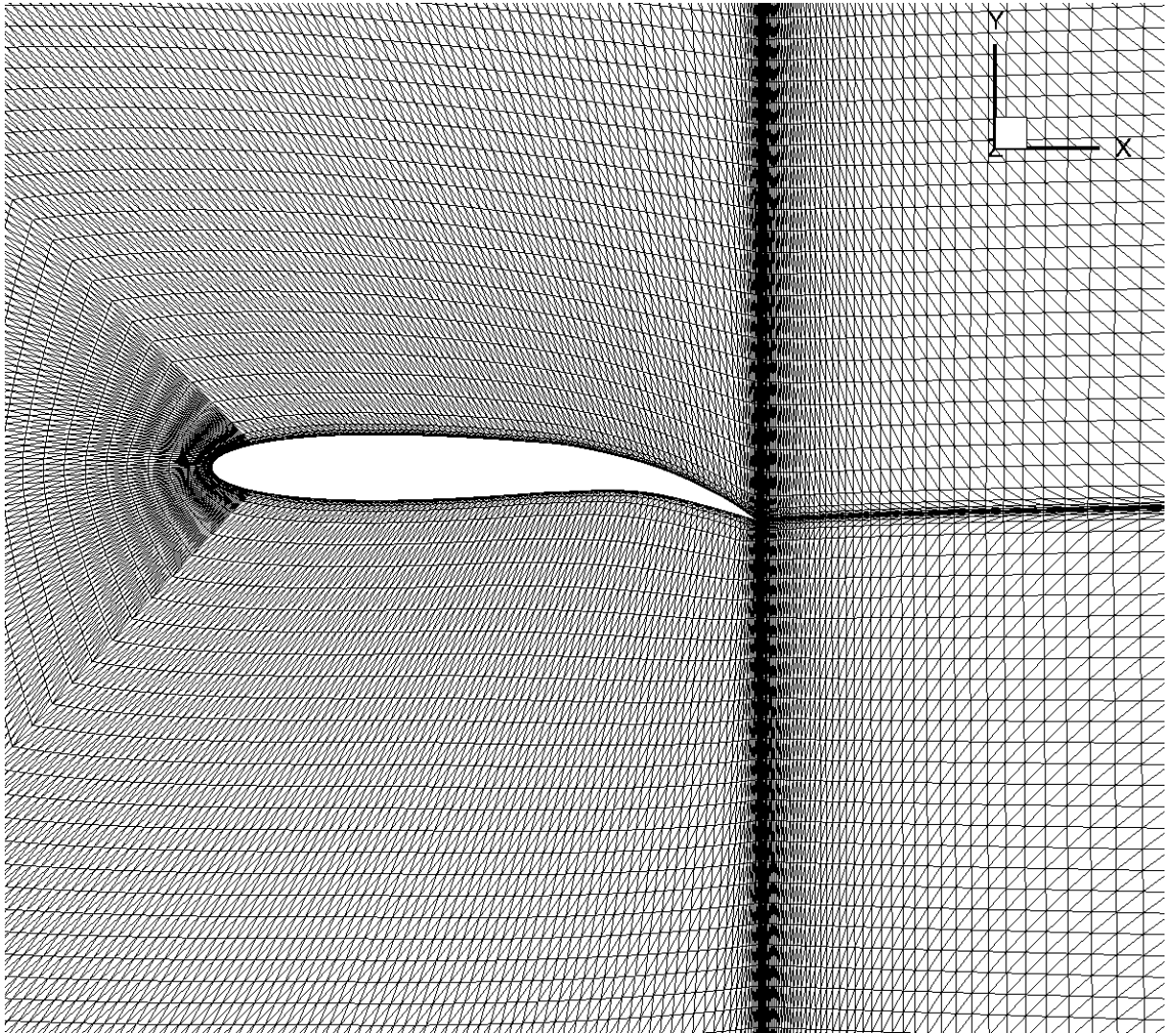


Figure 36: the mesh around the airfoil when it has morphed completely downward

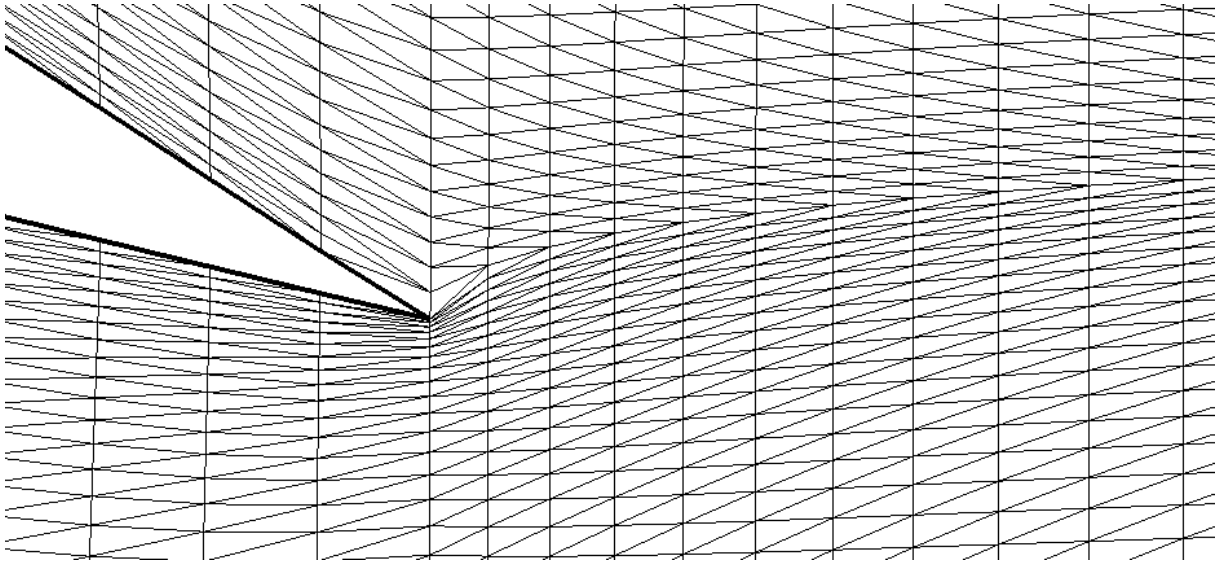


Figure 37: the mesh around the tail when the airfoil is deformed completely downward

## 6.4 Setup

In these simulations, the Mach number is 0.1. This Mach number is used to calculate the velocity of the incoming flow. The Reynolds number is maintained at 10,000. In these cases, smoothing is performed using the spring method.

The CFL number for this simulation was started at 1 and was allowed to increase at each iteration to a value of 100. This was found to be the highest CFL number that could be used without any negative volumes appearing in the mesh. Up to 500 inner loop iterations are completed for each cycle.

## 6.5 Deformed Mesh Coordinates

The Fourier equations for the shape of each frame of the deformed airfoil are determined using the coordinates for the points provided by Pankonien et al., and included in a subroutine in the in-house code. The user inputs the number of iterations in between the frames - for these simulations, that number is 200. The code has this number of iterations to get the points along the airfoil shape line to the next specified

line. This movement is done linearly between the points.

The speed of the deformation is not constant between each frame. When the airfoil is deforming downward, it deforms to a higher angle in a smaller number of frames and thus deforms in this direction more quickly.

## 6.6 Convergence

The linear residual criteria inside GMRES is  $1 \times 10^{-6}$ . A total of six cycles were run. This number is low but is limited by the resources available and the time required to complete each cycle: using Compute Canada's high-performance computers, each cycle took approximately one week using 144 processors.

## 6.7 Results

The images in Figure 38 show the vortices created behind the morphing airfoil at each of the extreme deformation locations, along with the airfoil in its undeformed state. The undeformed state of the airfoil is Frame 14, shown in the center of Figure 38, while the downward deformation is shown on the left is Frame 21 and the upward deformation shown on the right is Frame 1. The images in Figure 39 show the streamlines of the vortices created behind the deforming airfoil at each of the extreme deformation locations, along with the airfoil in its undeformed state. It is interesting to see how the deformation of the trailing edge corresponds to changes in pressure at the leading edge of the airfoil.

### 6.7.1 Aerodynamic Forces based on Time

Figure 40 shows how the lift and drag coefficients vary with time for one cycle.

Both the lift and drag peak just after halfway through the cycle. This corresponds

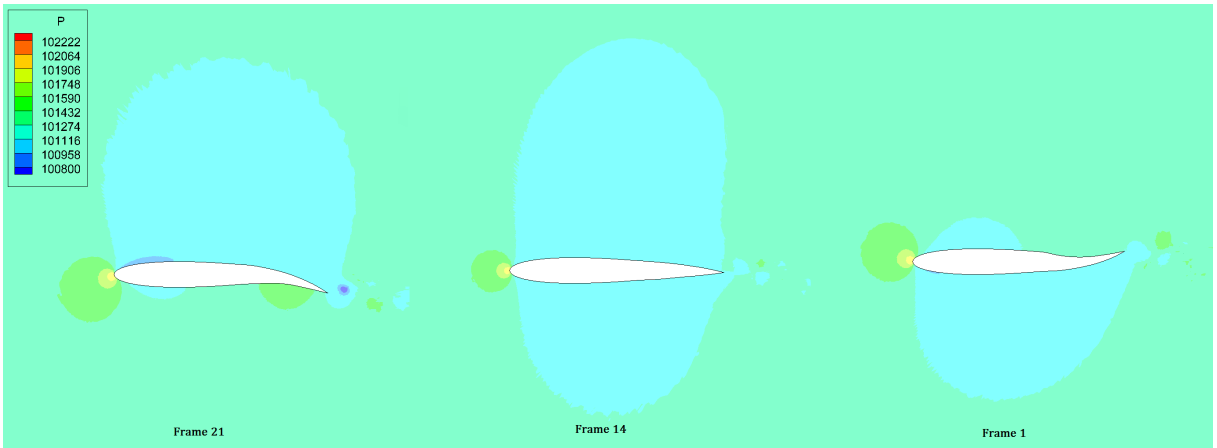


Figure 38: pressure contours around the deforming airfoil

to Frame 21 of the deforming airfoil, the first position shown in Figure 38, and the top airfoil shown in Figure 39. At this stage of the deformation, there is a large area of low pressure above the airfoil and atmospheric pressure below it. There is low pressure at the leading edge, and two vortices at the tail, both of which create low pressure.

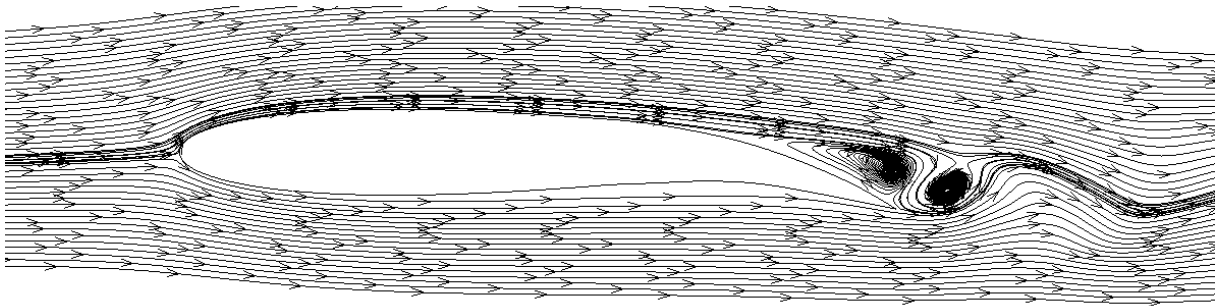
It is interesting to note that not much occurs when the airfoil deforms upward to Frame 1. This is likely because this creates vortices on either side of the airfoil, and the changes in lift and drag generated by these cancel each other out.

These lift and drag curves correspond to the  $C_p$  graphs shown in Figure 41. Increasing the deformation of the airfoil increases the range of the pressure coefficient. The  $C_p$  curves for Frames 1 and 21 are similar in overall shape, but Frame 21 has a more significant pressure variation corresponding to having a larger area of low pressure near the trailing edge.

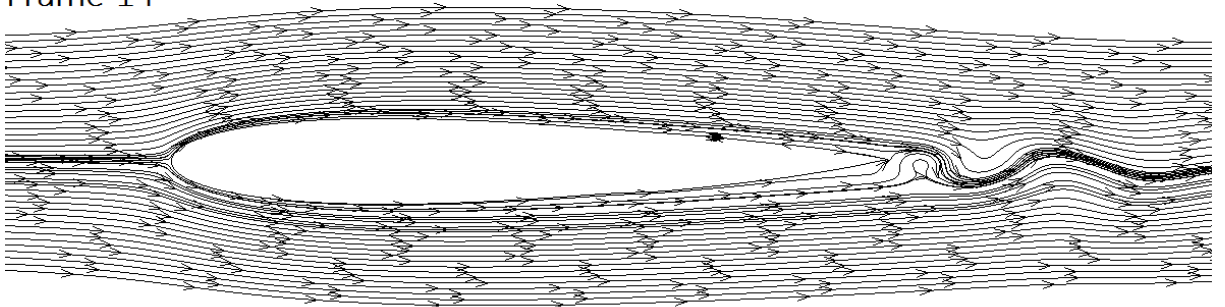
## 6.8 Deformation with Oscillation

With both deforming and oscillating cases completed, simulations can be run combining the two. The following simulation has the deformed airfoil oscillate from an

Frame 21



Frame 14



Frame 1

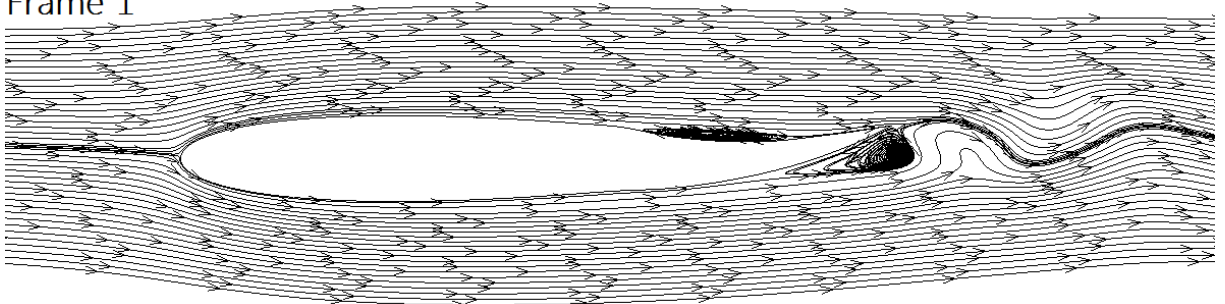


Figure 39: streamlines around the deforming airfoil

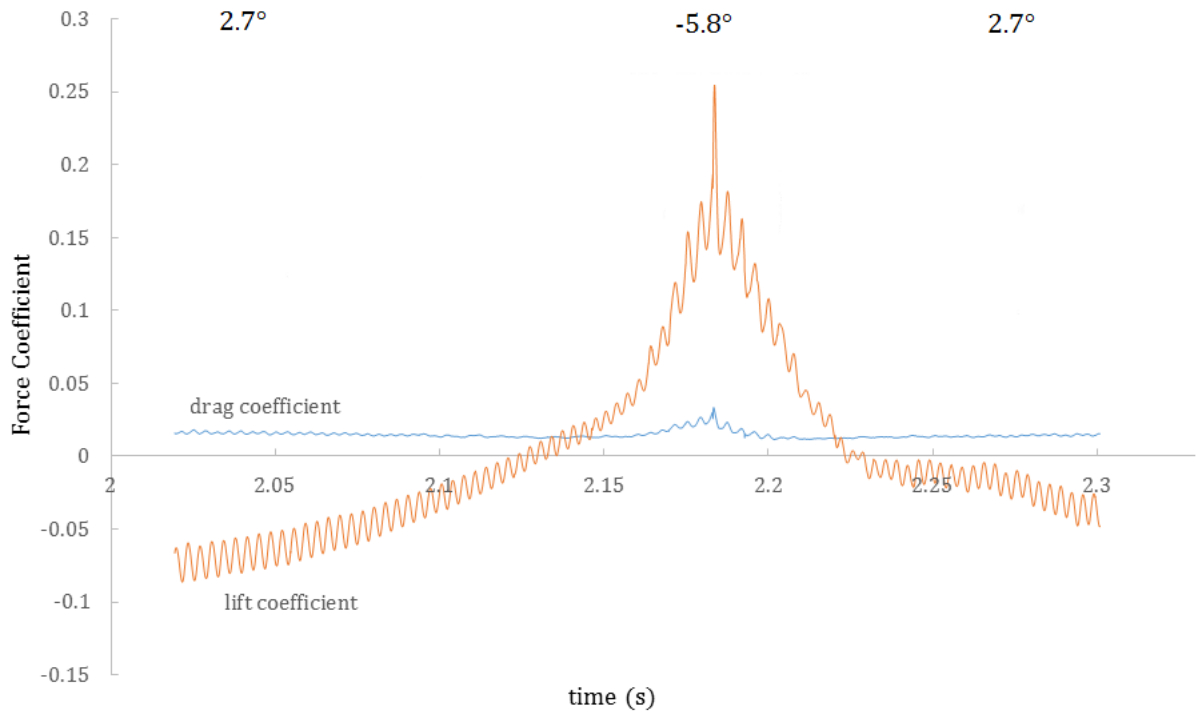


Figure 40: lift and drag coefficients with time for one cycle

angle of attack of  $0^\circ$  to  $20^\circ$ . This is done using the same geometry, domain, mesh, boundary conditions and convergence criteria presented for the deforming case, but the whole domain is rotated like in the oscillating case.

For this case, the airfoil is deformed to Frame 1. This was chosen because the lack of effects of the upward deformation on the lift and pressure coefficients was surprising and worthy of additional investigation.

### 6.8.1 Oscillating a Deformed Airfoil

The images in Figure 42 show the streamlines behind the deformed and dynamically oscillated airfoil.

The streamlines show the much larger vortices are when the airfoil is deformed to Frame 1 compared to how large they were when the airfoil was a symmetric NACA0012, in Figures 25 and 26. While initially at  $0^\circ$  angle of attack, there is

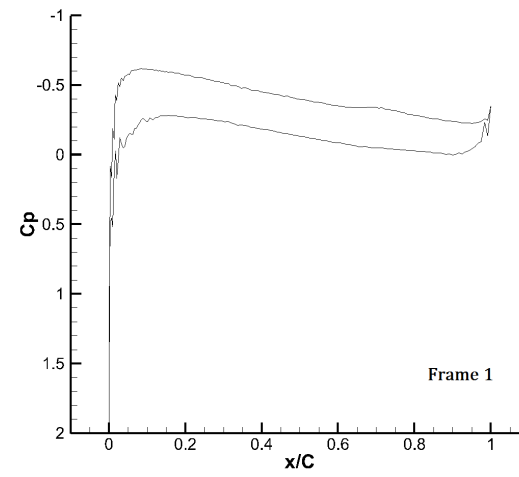
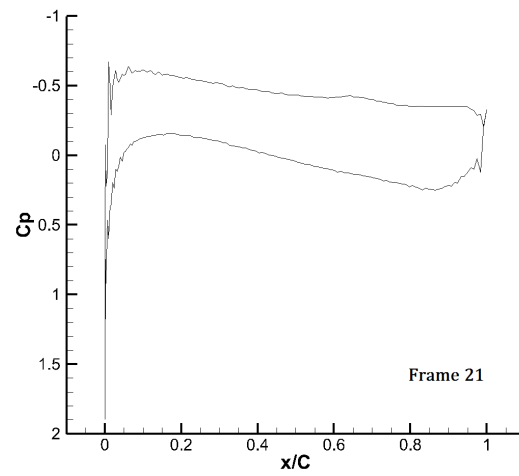
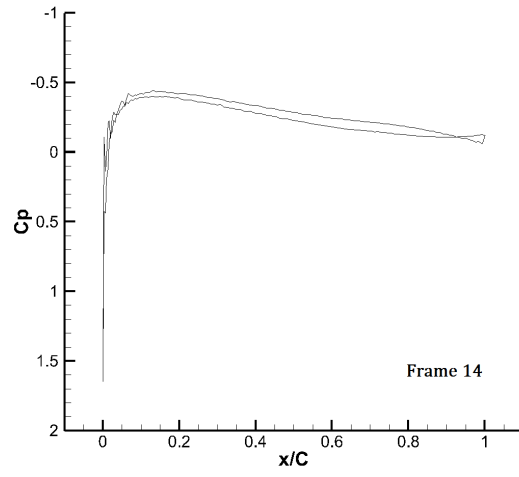


Figure 41: pressure coefficient with airfoil chord

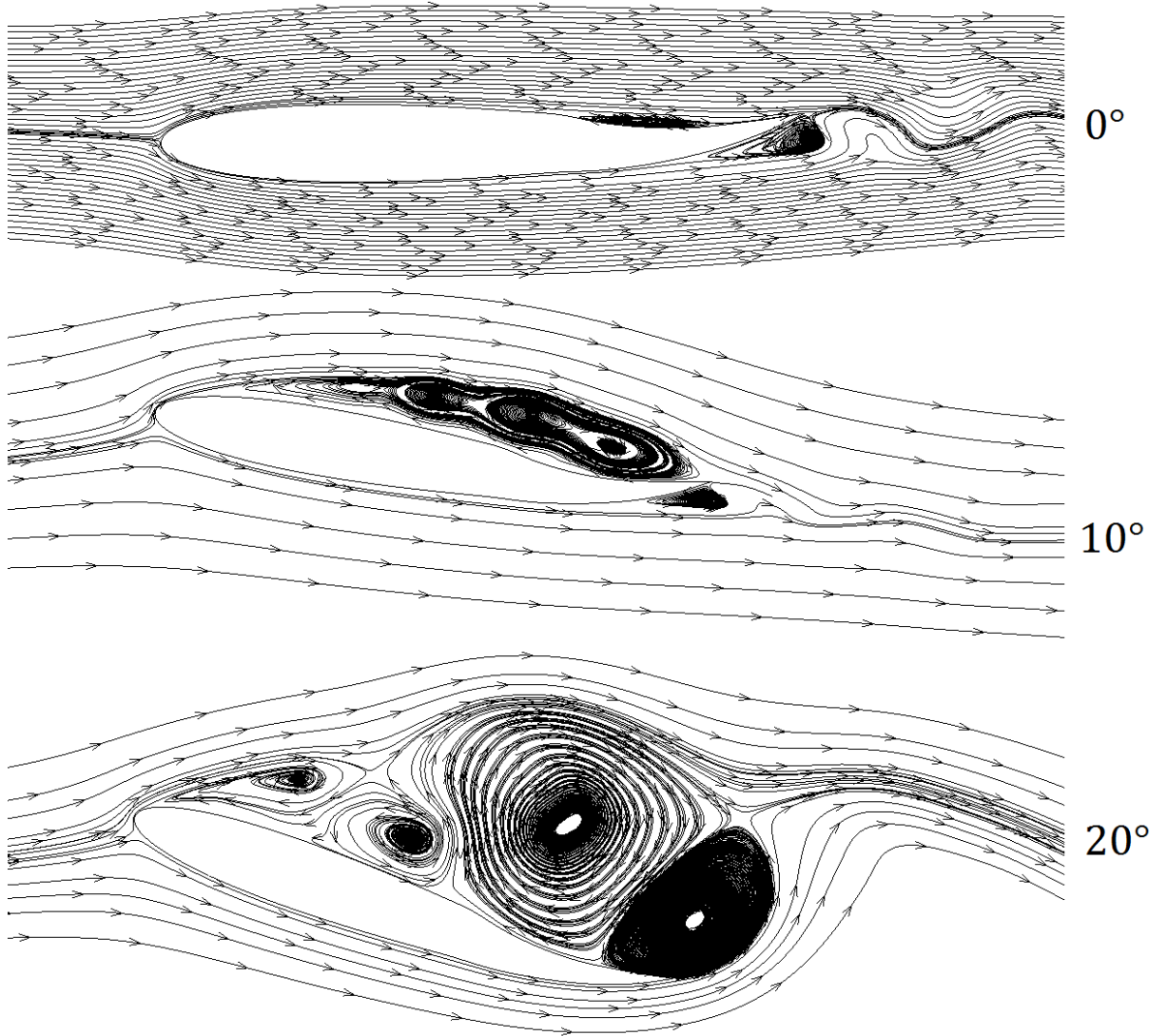


Figure 42: streamlines around an airfoil oscillated between 0 and 20 degrees

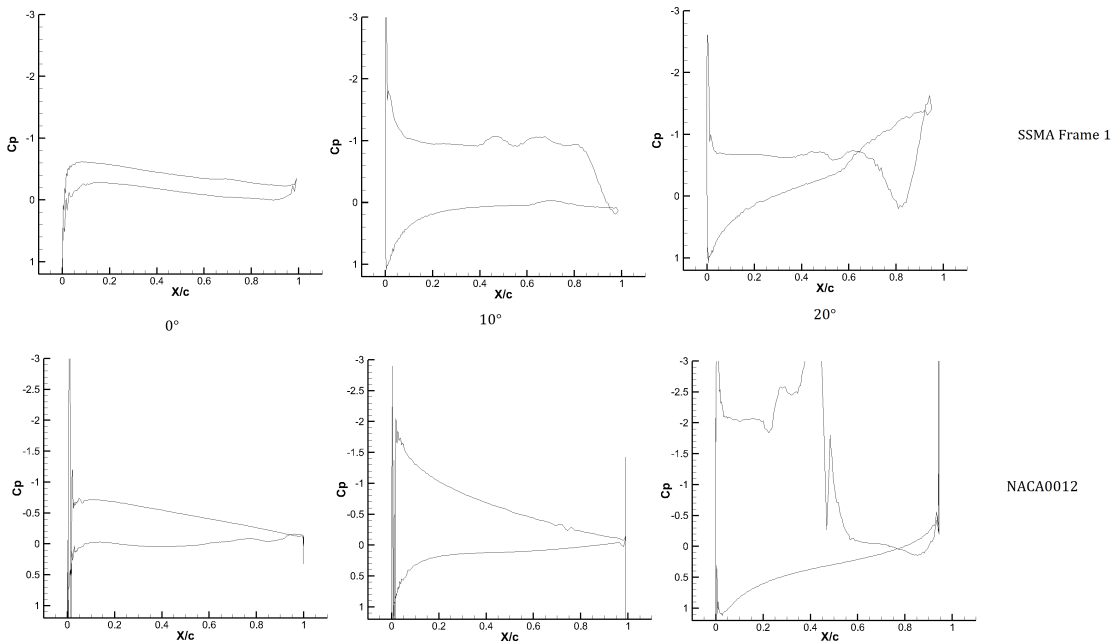


Figure 43: comparing  $C_p$  curves for the deformed airfoil and the NACA0012

a vortex above and below the airfoil, as the airfoil oscillates the lower vortex shrinks and then moves up to the suction side. The vortices are not able to follow the airfoil because the deformation blocks them at the trailing edge. These results are significant because they show the ability of the code to capture the vortices produced by the unsteady flow.

Figure 43 compares the pressure coefficient curves of the deformed airfoil with the NACA0012. At a  $0^\circ$  angle of attack the two curves are quite similar. At  $10^\circ$ , the pressure gradient at the deformed airfoil is wider, corresponding to the higher number of vortices on the suction side of the airfoil. At a  $20^\circ$  angle of attack, the flow below the airfoil accelerates lowering the pressure there, reducing the pressure gradient and reversing the flow. Of these three angles, the deformed airfoil's best performance is at  $10^\circ$ : there, the pressure gradient is larger than it is for the NACA0012, and the vortex rotating in the opposite direction to the others is very small.

# Chapter 7

## Conclusions and Future Work

This thesis investigated the use of in-house LES code for complicated, moving boundary, unsteady flows. The main aerodynamic features of oscillating and deforming airfoils at a Reynolds number of 10,000 were captured.

For the oscillating case, the main features of the flow were well captured showing that the code can predict the dynamic stall vortex. A small difference was observed between experiment and simulation: vortices appeared to develop faster in the simulations than in the experiment. In the future, the simulations should be repeated using a matching turbulence intensity and rotation point.

Dynamic mesh methods were implemented, and the code was able to deform the mesh while maintaining its quality using a spring-based smoothing method. The aerodynamic difference between a NACA0012 and its deforming equivalent is that the deforming airfoil has vortices that are generated around it even when it is at an angle of attack of  $0^\circ$ . When the deformed airfoil is oscillated downward, the flow is not able to follow the curve of the airfoil and is trapped by the deformed trailing edge, creating a very different pressure coefficient compared to a NACA0012.

The results are limited by the resource intensiveness of the LES simulations. Additional cycles should be carried out for both cases. In particular, at present, there

is only one oscillating cycle to analyze, which was performed after two Euler cycles, and the deformed airfoil is only oscillated  $20^\circ$ .

This information can be applied to VAWT design because it shows that LES is a useful tool for VAWT aerodynamic simulation: the main features of the flow can be captured. It also shows the aerodynamics of a dynamically deforming airfoil, and the effects on the airfoil's pressure distribution. Finally, it demonstrates the need to correctly estimate the amount of incoming turbulence to accurately model a VAWT, which is challenging for VAWTs in urban environments.

It should be noted that this deforming airfoil was designed for aircraft applications: it is likely that a deforming airfoil explicitly intended for VAWTs would have different levels of camber and more optimized power output.

Implementing a deforming airfoil would add moving parts to a wind turbine, increasing its manufacturing and maintenance costs. A detailed analysis would have to be performed to determine whether the increase in power output would recoup the additional maintenance and manufacturing costs. In any case, like most technology, implementing a deforming airfoil should decrease in cost with time.

To bring the simulations to best represent real lift, multiple airfoils in VAWT configuration should be made to oscillate, deform, and rotate 360 degrees - but this is likely too expensive to be simulated with LES at present. The simulations could also be performed at a more typical Reynolds number for VAWTs: this would be between  $1.66 \times 10^4 < Re < 1.73 \times 10^5$  [47]. Finally, fully 3D models, instead of 2.5D models, could be used for the most representative results.

# Bibliography

- [1] *Aerodynamics of Wind Turbines.*, pages 83 – 140. John Wiley and Sons, Inc., 2002.
- [2] *Introduction: Modern Wind Energy and its Origins.*, pages 1 – 20. John Wiley and Sons, Inc., 2002.
- [3] Allet A. and Paraschivoiu I. Viscous flow and dynamic stall effects on vertical-axis wind turbines. *International Journal of Rotating Machinery, Vol 2, Iss 1, Pp 1-14 (1995)*, (1):1, 1995.
- [4] M. Akorede, H. Hizam, M. Ab Kadir, I. Aris, and S. Buba. Mitigating the anthropogenic global warming in the electric power industry. *Renewable and Sustainable Energy Reviews*, 16(5):2747 – 2761, Feb 2012.
- [5] J. Anderson. *Fundamentals of Aerodynamics*. McGraw-Hill Education, 2017.
- [6] ANSYS, Inc. *ANSYS Fluent Theory Guide*, 12.0 edition.
- [7] C. Argyropoulos and N. Markatos. Review: Recent advances on the numerical modelling of turbulent flows. *Applied Mathematical Modelling*, 39:693 – 732, 2015.
- [8] T. Barker, I. Bashmakov, L. Bernstein, J. Bogner, P. Bosch, R. Dave, and et al. Technical summary, in climate change 2007: mitigation. contribution of working group iii to the fourth assessment report of the intergovernmental panel on

- climate change. Technical report, Intergovernmental Panel on Climate Change, Cambridge, 2007.
- [9] National Energy Board. Canada’s energy future 2016. Technical report, Government of Canada, Ottawa, 2016.
- [10] F. Bos, B. van Oudheusden, and H. Bijl. Radial basis function based mesh deformation applied to simulation of flow around flapping wings. *Computers and Fluids*, 79:167–177, 2013.
- [11] A. Buchner, M. Lohry, L. Martinelli, J. Soria, and A. Smits. Dynamic stall in vertical axis wind turbines: Comparing experiments and computations. *Journal of Wind Engineering and Industrial Aerodynamics*, 146:163–171, 2015.
- [12] L. Carr. Progress in analysis and prediction of dynamic stall. *Journal of Aircraft*, 25(1):6–17, 1988.
- [13] L. Carr and M. Chandrasekhara. Compressibility effects on dynamic stall. *Progress in Aerospace Sciences*, 32(6):523 – 573, 1996.
- [14] A. Choudhry, R. Leknys, M. Arjomandi, and R. Kelso. An insight into the dynamic stall lift characteristics. *Experimental Thermal and Fluid Science*, 58:188–208, 2014.
- [15] G. Corcos and F. Sherman. The mixing layer: deterministic models of a turbulent flow. part 1. introduction and the two-dimensional flow. *Journal of Fluid Mechanics*, 139:29–65, 1984.
- [16] B. Cushman-Roisin and J. Beckers. *Introduction to Geophysical Fluid Dynamics: Physical and Numerical Aspects*. Academic Press. Academic Press, 2011.

- [17] A. de Boer, M. van der Schoot, and H. Bijl. Mesh deformation based on radial basis function interpolations. *Computers and Structures*, 85(11-14):784–795, 2007.
- [18] R. Dwight. Robust mesh deformation using the linear elasticity equations. In *Computational Fluid Dynamics 2006*, pages 401–406, 2009.
- [19] J. Ekaterinaris. Numerical investigation of dynamic stall of an oscillating wing. *AIAA Journal*, 33(10):1803–1808, 1995.
- [20] Goddard Institute for Space Studies. Giss surface temperature analysis, 2018.
- [21] T. Fransson. *Unsteady Aerodynamics and Aeroelasticity of Turbomachines*. Springer Science and Business Media, 1997, 1997.
- [22] K. Fujii. Progress and future prospects of cfd in aerospace - wind tunnel and beyond. *Progress in Aerospace Sciences*, 41(6):455 – 470, 2005.
- [23] N. Fujisawa and S. Shibuya. Observations of dynamic stall on darrieus wind turbine blades. *Journal of Wind Engineering and Industrial Aerodynamics*, 89(2):201–214, 2001.
- [24] Siemens Gamesa. Siemens gamesa to install two large onshore wind farm projects in south africa. *Siemens Gamesa Newsroom for Press and Media*, July 2018.
- [25] E. Garnier, N. Adams, and P. Sagaut. *Large eddy simulation for compressible flows*. Springer, 9 edition, 2009.
- [26] W. Geissler and B. van der Wall. Dynamic stall control on flapping wing airfoils. *Aerospace Science and Technology*, 62:1 – 10, 2017.
- [27] K. Gharali and D. Johnson. Dynamic stall simulation of a pitching airfoil under unsteady freestream velocity. *Journal of Fluids and Structures*, 42:228 – 244, 2013.

- [28] N. Gillaud, G. Balarac, and E. Goncalvs. Large eddy simulations on a pitching airfoil: Analysis of the reduced frequency influence. *Computers and Fluids*, 161:1–33, 2018.
- [29] C. Greenwood, A. Hohler, G. Hunt, M. Liebreich, V. Sonntag-O'Brien, and E. Usher. Global trends in sustainable energy investment 2007–analysis of trends and issues in the financing of renewable energy and energy efficiency in oecd and developing countries. In *Untersuchung im Auftrag des United Nations Environment Programme*. United Nations, 2007.
- [30] T. Gmen, P. van der Laan, P. Rthor, A. Diaz, G. Larsen, and S. Ott. Wind turbine wake models developed at the technical university of denmark: A review. *Renewable and Sustainable Energy Reviews*, 60:752 – 769, 2016.
- [31] B. Hand, G. Kelly, and A. Cashman. Numerical simulation of a vertical axis wind turbine airfoil experiencing dynamic stall at high reynolds numbers. *Computers and Fluids*, 149:12–30, 2017.
- [32] D. Hefeng, W. Chenxi, L. Shaobin, and S. Xi Zhen. Numerical research on segmented flexible airfoils considering fluid-structure interaction. *Procedia Engineering*, 99:57–66, 2015.
- [33] SAWT Inc. Pk10-ab. *SAWT Product List*, 2013.
- [34] Cambridge-MIT Institute. Naca0012. *CMI Multidisciplinary Design Project*.
- [35] IRENA. Global energy transformation: A roadmap to 2050. Technical report, International Renewable Energy Agency, Abu Dhabi, 2018.
- [36] G. Jones, M. Santer, M. Debiasi, and G. Papadakis. Control of flow separation around an airfoil at low reynolds numbers using periodic surface morphing. *Journal of Fluids and Structures*, 76:536–557, 2018.

- [37] M. Kerho. Adaptive airfoil dynamic stall control. *Journal of Aircraft*, 44(4):1350–1360, 2007.
- [38] A. Kolmogorov. The local structure of turbulence in incompressible viscous fluid for very large reynolds’ numbers. In *Dokl. Akad. Nauk USSR*, volume 30, pages 301–305, 1941.
- [39] M. Komeili. *Large Eddy Simulation of Vertical Axis Wind Turbine for Low Reynolds Number Applications*. PhD thesis, Concordia University, Montreal, 2016.
- [40] R. Kumar, K. Raahemifar, and A. Fung. A critical review of vertical axis wind turbines for urban applications. *Renewable and Sustainable Energy Reviews*, 89:281 – 291, 2018.
- [41] T. Lee and P. Gerontakos. Investigation of flow over an oscillating airfoil. *Journal of Fluid Mechanics*, 512:313341, 2004.
- [42] J. Leishman and T. Beddoes. A semi-empirical model for dynamic stall. *Journal of the American Helicopter Society*, 34(3):3–17, 1989.
- [43] Q. Li, T. Maeda, Y. Kamada, J. Murata, K. Furukawa, and M. Yamamoto. The influence of flow field and aerodynamic forces on a straight-bladed vertical axis wind turbine. *Energy*, 111:260 – 271, 2016.
- [44] S. Li, S. Wang, J. Wang, and J. Mi. Effect of turbulence intensity on airfoil flow: Numerical simulations and experimental measurements. 32:1029–1038, 08 2011.
- [45] W. McCroskey. Unsteady airfoils. *Annual Review of Fluid Mechanics*, 14:285–311, 1982.
- [46] W. McCroskey, L. Carr, and K. McAlister. Dynamic stall experiments on oscillating airfoils. *AIAA Journal*, 14(1):57–63, 1976.

- [47] M. Miller, S. Duvvuri, I. Brownstein, M. Lee, J. Dabiri, and M. Hultmark. Vertical-axis wind turbine experiments at full dynamic similarity. *Journal of Fluid Mechanics*, 844:707720, 2018.
- [48] K. Mulleners and M. Raffel. Dynamic stall development. *Exp Fluids*, 54:1–9, 2013.
- [49] B. Munson, D. Young, and T. Okiishi. *Fundamentals of Fluid Mechanics*. John Wiley and Sons, Hoboken, 4 edition, 2002.
- [50] F. Nicoud and F. Ducros. Subgrid-scale stress modelling based on the square of the velocity gradient tensor. *Flow, Turbulence and Combustion*, 62:193–200, 1999.
- [51] A. Pankonien, C. Faria, and D. Inman. Synergistic smart morphing aileron. In *54th AIAA/ASME/ASCE/AHS/ASC Structures, Structural Dynamics, and Materials Conference*, Boston, 2013.
- [52] M. Secanell, A. Suleman, and P. Gamboa. Design of a morphing airfoil using aerodynamic shape optimization. *AIAA Journal*, 44(7):1550–1562, 2006.
- [53] A. Shires. Design optimisation of an offshore vertical axis wind turbine. *Institution of Civil Engineers*, 166(EN1):7–18, 2012.
- [54] A. Spentzos, G. Barakos, K. Badcock, B. Richards, P. Wernert, S. Schreck, and M. Raffel. Investigation of three-dimensional dynamic stall using computational fluid dynamics. *AIAA Journal*, 43(5):1023–1033, 2005.
- [55] J. Tan. Simulation of morphing blades for vertical axis wind turbines. Master’s thesis, Concordia University, Montreal, 2017.

- [56] C. Tseng and Y. Cheng. Numerical investigations of the vortex interactions for a flow over a pitching foil at different stages. *Journal of Fluids and Structures*, 58:291–318, 2015.
- [57] C. Viozat. Implicit upwind schemes for low mach number compressible flows. Technical report, INRIA, 1997.
- [58] G. Wang, L. Zhang, and W. Shen. Les simulation and experimental validation of the unsteady aerodynamics of blunt wind turbine airfoils. *Energy*, 158:911 – 923, 2018.
- [59] S. Wang, D. Ingham, L. Ma, M. Pourkashanian, and Z. Tao. Turbulence modeling of deep dynamic stall at relatively low reynolds number. *Journal of Fluids and Structures*, 33:191 – 209, 2012.
- [60] A. Zanotti, R. Nilifard, G. Gibertini, A. Guardone, and G. Quaranta. Assessment of 2d/3d numerical modeling for deep dynamic stall experiments. *Journal of Fluids and Structures*, 51:97 – 115, 2014.
- [61] X. Zhang and J. Schlter. Numerical study of the influence of the reynolds-number on the lift created by a leading edge vortex. *Physics of Fluids*, 24(6):065102, 2012.
- [62] Y. Zhiyin. Large-eddy simulation: Past, present and the future. *Chinese Journal of Aeronautics*, 28(1):11 – 24, 2015.

# Appendix

## Deforming Airfoil Frames

The following figures show the shape of the deforming airfoil at each of the 21 frames provided by Pankonien et al. [51]. Pankonien et al. provided a set of data points. These data points were used to create a Fourier equation with the following form:

$$\begin{aligned}
 y = & a_0 + a_1 \cos(x \cdot ww) + b_1 \sin(x \cdot ww) + a_2 \cos(2x \cdot ww) + b_2 \sin(2x \cdot ww) \\
 & + a_3 \cos(3x \cdot ww) + b_3 \sin(3x \cdot ww) + a_4 \cos(4x \cdot ww) + b_4 \sin(4x \cdot ww) \\
 & + a_5 \cos(5x \cdot ww) + b_5 \sin(5x \cdot ww) + a_6 \cos(6x \cdot ww) + b_6 \sin(6x \cdot ww) \quad (46)
 \end{aligned}$$

The variables shown in the equation are different for the three main frames.

	<b>Frame 1</b>	<b>Frame 1</b>	<b>Frame 14</b>	<b>Frame 14</b>	<b>Frame 21</b>	<b>Frame 21</b>
Coefficient	Upper	Lower	Upper	Lower	Upper	Lower
$a_0$	11.06	-4.249	7.753	-8.962	157.2	-19.45
$a_1$	4.702	-12.74	5.979	-6.336	-46.89	8.746
$b_1$	-0.6053	4.657	-4.307	2.373	279.6	2.032
$a_2$	0.09625	6.147	-3.697	2.854	-210.6	-2.478
$b_2$	-0.05436	0.01053	0.4255	0.9047	-41.76	-1.541
$a_3$	-0.2032	-2.498	1.928	-0.6269	29.98	-0.1496
$b_3$	-0.1146	-1.833	0.7825	-1.493	-119.7	1.365

$a_4$	-0.1349	0.4049	-0.6374	-0.3204	50.61	0.5221
$b_4$	-0.1641	1.256	-0.7667	0.6059	15.63	-0.4167
$a_5$	-0.01439	0.09634	0.1024	0.2771	-5.49	-0.2742
$b_5$	-0.02163	-0.5205	0.458	-0.128	14.55	-0.1122
$a_6$	0.05231	-0.1105	0.01691	-0.09244	-2.076	-0.02947
$b_6$	0.03344	0.09837	-0.1259	-0.04532	-1.077	0.103
$ww$	0.039	0.03066	0.02889	0.03137	0.0209	0.03097

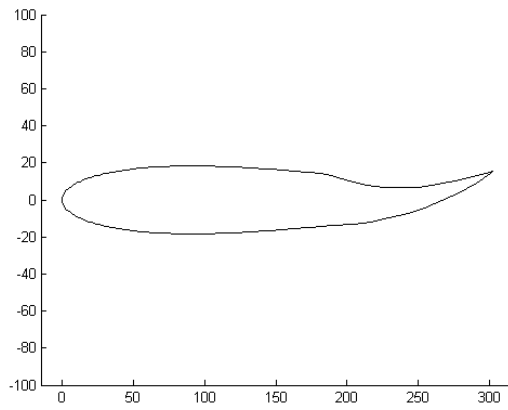


Figure 44: Frame 1

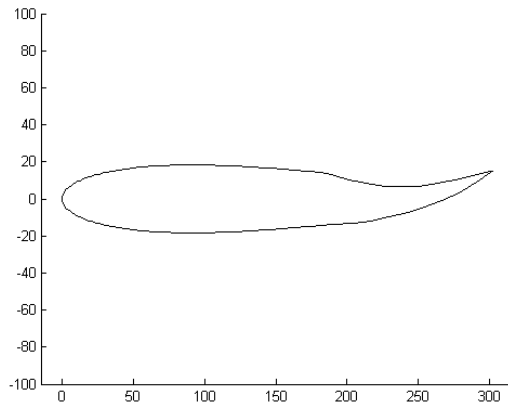


Figure 45: Frame 2

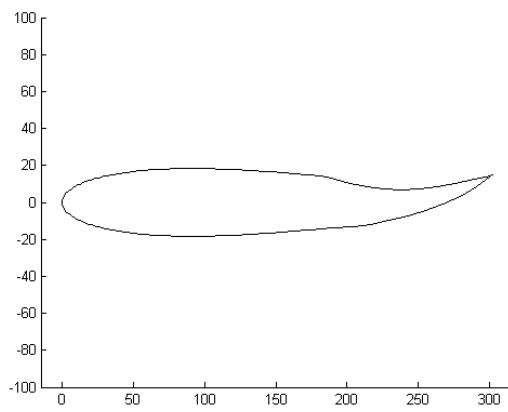


Figure 46: Frame 3

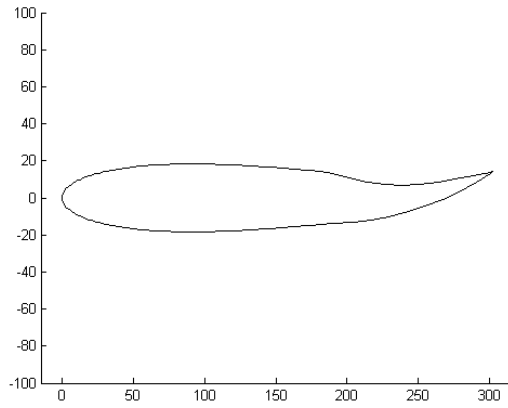


Figure 47: Frame 4

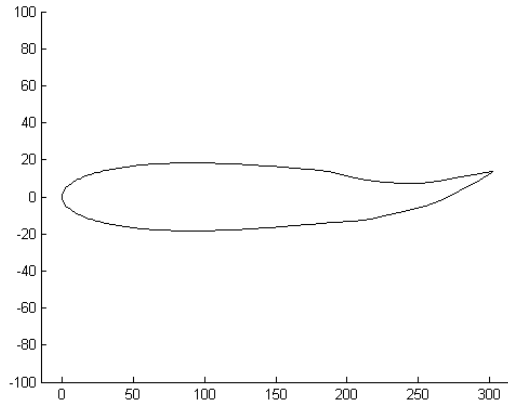


Figure 48: Frame 5

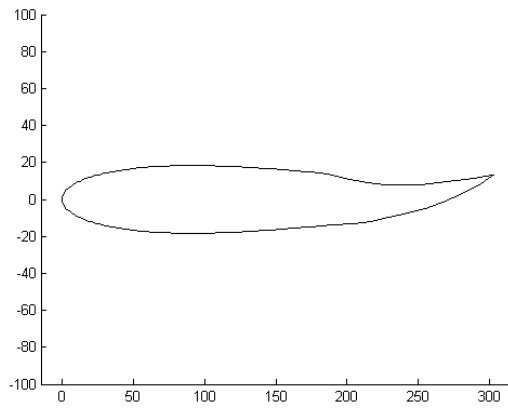


Figure 49: Frame 6

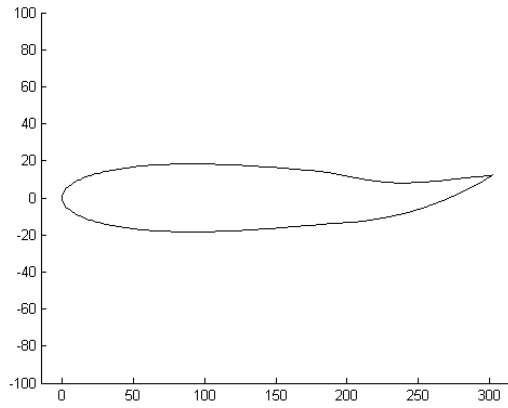


Figure 50: Frame 7

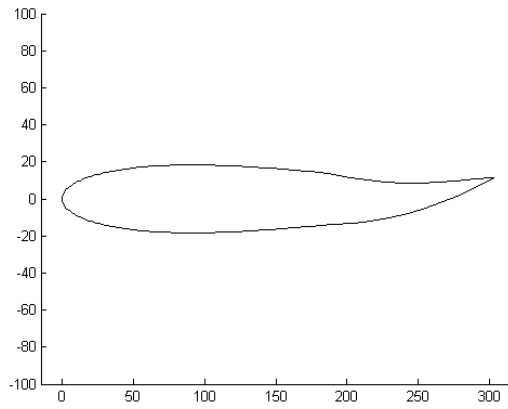


Figure 51: Frame 8

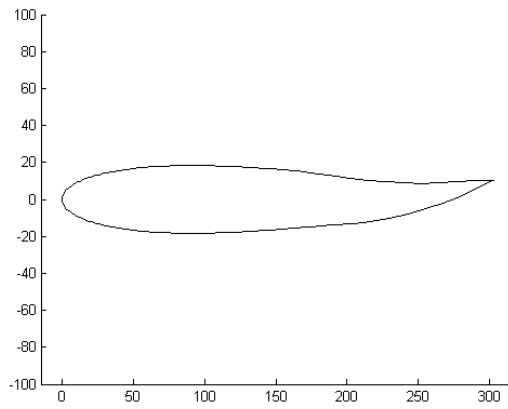


Figure 52: Frame 9

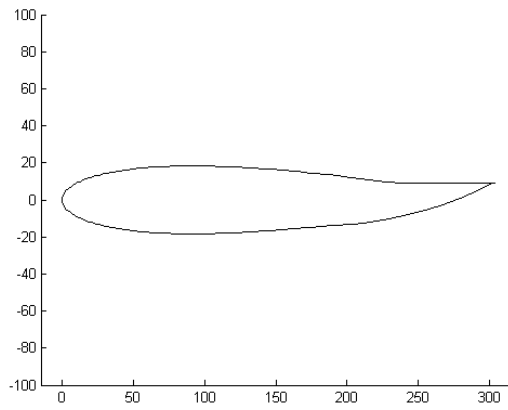


Figure 53: Frame 10

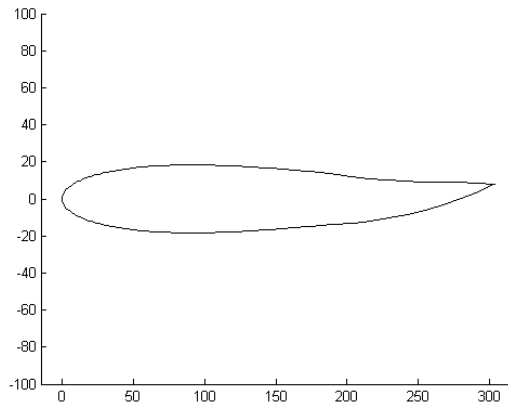


Figure 54: Frame 11

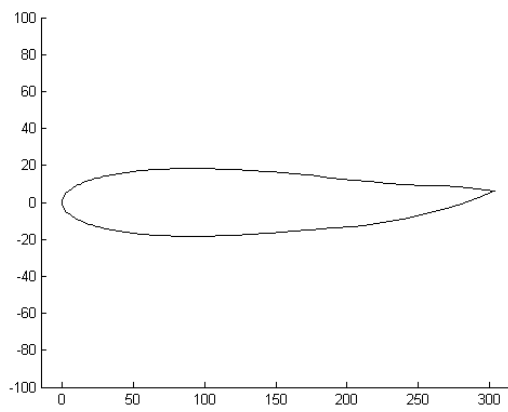


Figure 55: Frame 12

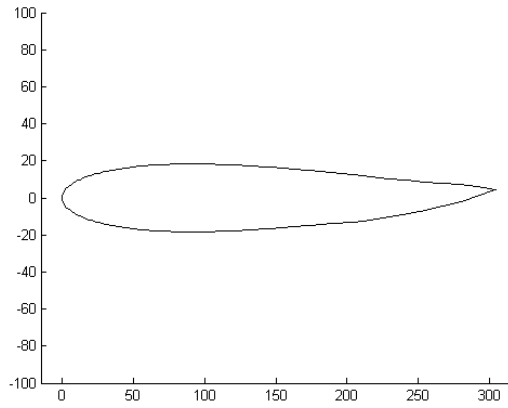


Figure 56: Frame 13

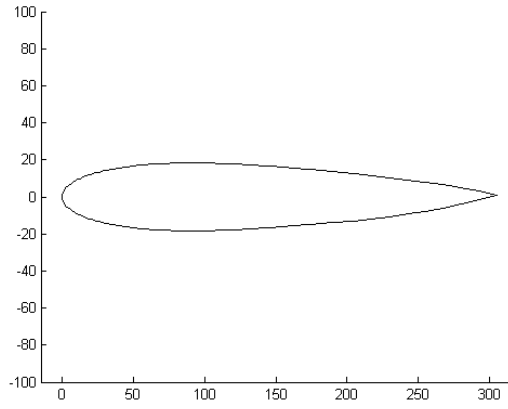


Figure 57: Frame 14

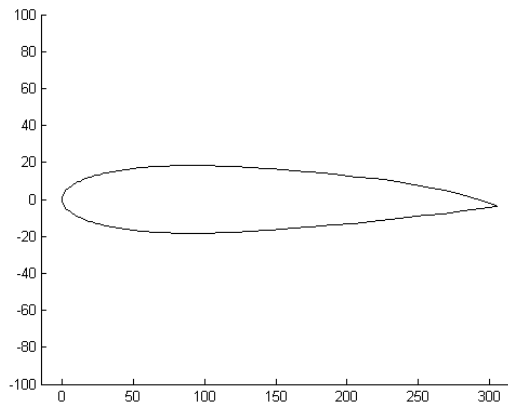


Figure 58: Frame 15

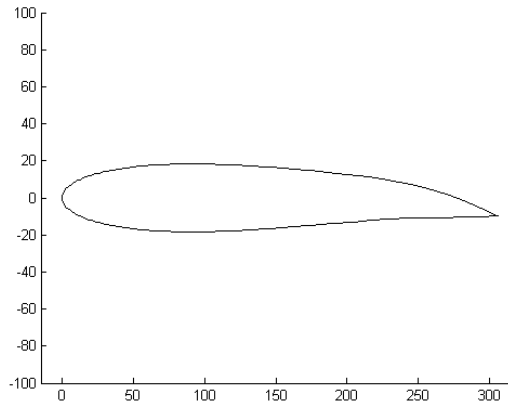


Figure 59: Frame 16

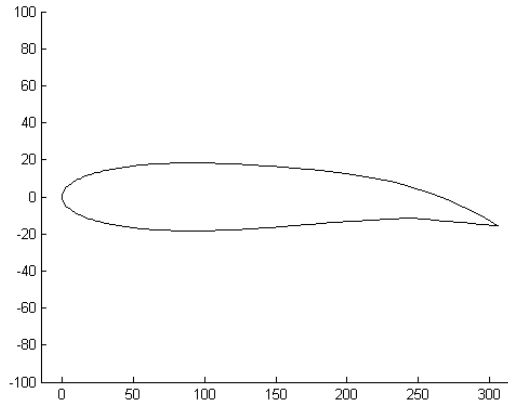


Figure 60: Frame 17

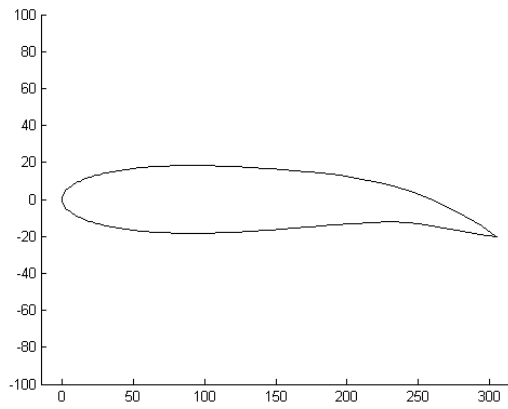


Figure 61: Frame 18

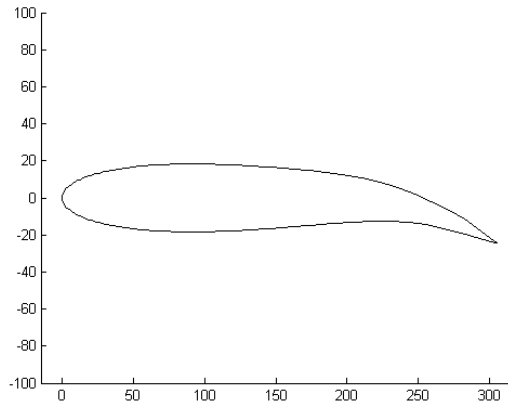


Figure 62: Frame 19

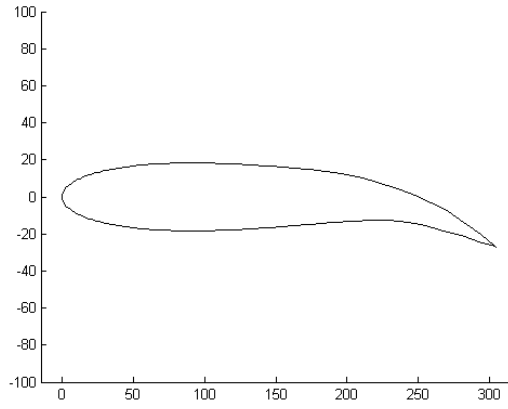


Figure 63: Frame 20

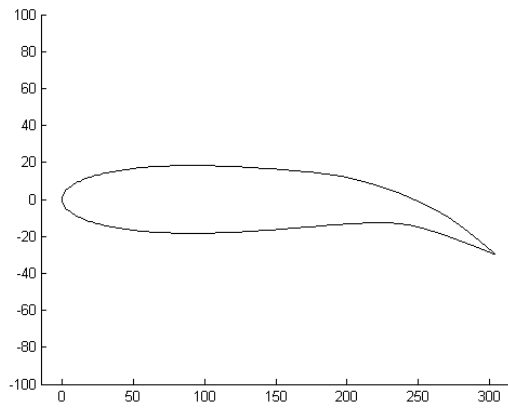


Figure 64: Frame 21